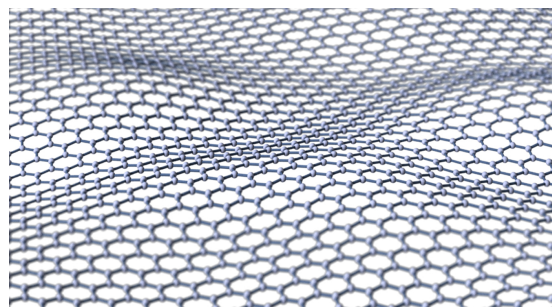


Research Internship (PRE)

Field of Study: SEM
Scholar Year: 2017-2018

Characterization of as-deposited and annealed Pt thin film grown on MgO(111), Al₂O₃(0001), SiO₂(2 nm)(001)/Si and SiO₂(300 nm)(001)/Si substrates by sputtering deposition



Confidentiality Notice
Non-confidential report and publishable on Internet

Author: Anbo CAO	Promotion: 2019
ENSTA ParisTech Tutor: Ziad MOUMNI	Host Organization Tutor: Johann CORAUX, Nicolas ROUGEMAILLE

Internship from 14/05/2018 to 09/08/2018

Name of the host organization: Institut Néel
Address: 25 Avenue des Martyrs
38042 Grenoble
France

Attestation de confidentialité
À remettre à la bibliothèque de l'ENSTA ParisTech
Rapport de Projet de Recherche (PRe)

Par la présente, je soussigné (e) **Madame** / Monsieur¹ NOM Prénom

CORAUX Johann

Employé(e) en tant que (qualité) **Chargé de recherche CNRS**

dans la société : NOM **Institut Néel**

ADRESSE de l'établissement :

25 rue des Martyrs, 38042 Grenoble Cedex 09

Atteste sur l'honneur que les données contenues dans le rapport de

Madame / Monsieur¹ NOM-Prénom **CAO Anbo** **sont :**

- Confidentielles.** Par conséquent, la communication du contenu à l'extérieur est strictement interdite. **Date de fin de confidentialité :** / /

Si le document est confidentiel cocher également le choix correspondant :

- L'entreprise autorise la mise en ligne des données bibliographiques (titre, auteur, nom entreprise...) du rapport sur le catalogue de la bibliothèque.
 L'entreprise n'autorise pas la mise en ligne des données bibliographiques (titre, auteur, nom entreprise...) du rapport sur le catalogue de la bibliothèque.

Non confidentielles. Cocher également le choix correspondant :

- L'entreprise autorise la mise en ligne du rapport de stage sans restriction sur Internet. **L'étudiant doit alors déposer son rapport sur BibNum.**
- L'entreprise autorise une mise en ligne restreinte du rapport de stage (via l'annuaire LDAP de l'école). **L'étudiant doit alors déposer son rapport sur BibNum.**
- L'entreprise autorise l'accès au document uniquement sur place et au format imprimé. **L'étudiant doit alors déposer son rapport en version papier à la bibliothèque.**

Si le rapport est consultable uniquement sur place, l'établissement autorise que les données bibliographiques² du rapport soient mises en ligne dans le catalogue de la bibliothèque.

Oui / Non

À **Grenoble**

Le **18. / 06. / 18..**

Signature et cachet

[Signature]
Institut NEEL
CNRS
Bâtiment : D
25, rue des Martyrs - BP 166
38042 Grenoble cedex 9

¹ Rayer la mention inutile

² Titre, auteur, tuteurs, nom de l'entreprise, nombre de pages.

Acknowledgment

I would like to express my gratitude to all those who helped me during my internship.

My deepest gratitude goes first and foremost to Dr. Johann Coraux, my supervisor, for his constant encouragement and guidance. During my internship he proposed the subject and the plan, and he helped a lot in the preparation of this thesis. Without his patient instruction, insightful criticism and expert guidance, the completion of this thesis would not have been possible.

Second, I would express my heartfelt gratitude to Dr. Nicolas Rougemaille. He offered me invaluable advice and informative suggestions. My study is an extension of the previous work done by Dr. Coraux and Dr. Rougemaille. What they had discovered has been useful to me.

I also owe a special debt of gratitude to all the researchers in Institut Néel, especially Dr. Eric Mossang, who helped me with X-ray diffraction, Dr. Philippe David, who taught me about sputtering deposition, and Dr. Simon Le-Denmat, who trained me to use atomic force microscopy.

Last but not the least, my gratitude also extends to my family who have been assisting, supporting and caring for me all of my life.

Abstract

Graphene has attracted much attention in the field of spintronics for its long spin diffusion length. Graphene/Co/Pt(111) has been studied and the magnetic anisotropy was found to be enhanced by the interaction between graphene and Co. To reduce the cost to prepare this promising material, the possibility to replace the bulk single-crystal Pt(111) with an epitaxial high quality Pt(111) thin film prepared on a commercial substrate is studied. Pt thin films with the thickness of 10 nm are grown on MgO(111), Al₂O₃(0001), SiO₂(2 nm)(001)/Si and SiO₂(300 nm)(001)/Si substrates by sputtering deposition. Atomic force microscopy (AFM) and X-ray diffraction (XRD) show that the thin films are very homogeneous and the roughness of the surface is low. The Pt/SiO₂(2 nm)(001)/Si and Pt/Al₂O₃(0001) samples are annealed in ultrahigh vacuum at 700K for 30 min. According to AFM and XRD characterization, the former undergoes dewetting and interdiffusion so that the Pt thin film is destroyed. High quality epitaxial Pt thin film with the (111) plane parallel to the substrate is grown on Al₂O₃(0001) after annealing. These thin films appear suitable for the growth of graphene with well-controlled crystallinity.

KEY WORDS : epitaxy; annealing; sputtering deposition; atomic force microscopy; X-ray diffraction.

Résumé

Le graphène a attiré beaucoup d'attention dans le domaine de la spintronique pour sa longueur de diffusion de spin. Le graphène/Co/Pt(111) système a été étudié et l'anisotropie magnétique s'est révélée améliorée par l'interaction entre graphène et Co. Pour réduire le coût de préparation de ce matériau prometteur, la possibilité de remplacer le Pt(111) massif monocristallin avec un film mince épitaxial de Pt(111) de haute qualité préparé sur un substrat commercial est étudiée. Des films minces de Pt ayant une épaisseur de 10 nm sont développés sur substrats MgO (111), Al₂O₃(0001), SiO₂(2 nm)(001)/Si et SiO₂(300 nm)(001)/Si par le dépôt de pulvérisation. La microscopie à force atomique (AFM) et la diffraction des rayons X (DRX) montrent que les couches minces sont très homogènes et que la rugosité de la surface est faible. Les échantillons Pt/SiO₂(2 nm)(001)/Si et Pt/Al₂O₃(0001) sont recuits sous ultravide à 700 K pendant 30 min. Selon la caractérisation AFM et XRD, le premier subit un démolillage et une interdiffusion au point de détruire le film mince de Pt. Un film mince épitaxial de haute qualité en Pt avec le plan (111) parallèle au substrat est mis en épitaxie sur Al₂O₃(0001) après recuit. Ce type de film semble adapté à la croissance de graphène de qualité cristalline contrôlée.

MOTS CLÉS: épitaxie; recuit; dépôt par pulvérisation; microscopie à force atomique; diffraction des rayons X.

Contents

Acknowledgment	4
Abstract	5
Contents	6
Introduction	7
I Scientific background	9
I.1 High quality thin film preparation	9
I.2 Large area CVD growth of graphene	12
II Experimental techniques	16
II.1 Sputtering deposition	16
II.2 AFM	17
II.3 XRD and XRR	18
II.4 Experiment process	20
III Results and discussion	21
III.1 Morphology of deposits	21
III.2 Crystal structure	26
Conclusion	33
Bibliography	34
Glossary	36
List of Tables	37
List of Figures	38

Introduction

Graphene is a promising material and its properties are still under research. Recently it attracts much attention in the field of spintronics for its long spin diffusion length.

Spin is an intrinsic value of elementary particles. A classical analogy of spin is to consider it as the rotation of the particle around its own axis. This analogy is not true since elementary particles do not rotate as solid objects, but spin in quantum mechanics resembles classical rotation in calculation. Spin has two directions : up and down. In a binary logic a circuit has two states, on and off. If the state of a circuit is combined with the spin of an electron, a four-state circuit is formed and this circuit carries more information. Compared with a two-state system, a four-state one has higher data transfer speed and bigger data storage capacity. By using a magnetic sensor to read data, it is possible to build the new generation hard disk on four-state system and this hard disk is likely to be more effective. All these advantages are guaranteed by the additional degree of freedom of electron.

Because of the extremely weak spin-orbit coupling and the absence of hyperfine interaction in ¹²C-graphene, graphene has the potential to be used in the realization of the four-state circuit [1, 2]. Micrometer-scale distance spin transport is observed in single layer graphene and no significant difference is found between 4.2 K, 77 K and room temperature [3]. In the highest-quality samples, the spin transport distance now reaches 3-12 μ m at 300 K [4], and charge density does not have a big influence on this length. In experiments the spin lifetime is between tens of picoseconds and a few nanoseconds. The spin injection efficiency from ferromagnetic cobalt electrodes to single layer graphene is as low as 10%, which is possibly due to a conductance mismatch between the electrode and the graphene layer or other contact-related effects. The efficiency is much higher by using magnesium oxide thin film as the tunnel barrier. Further study shows that the spin injection efficiency can be over 60% by tunneling across an insulating barrier [5]. Graphene also has high electron mobility, and a tunable charge carrier concentration.

The major challenge in building a four-state system with graphene is that graphene is strongly diamagnetic. In order to induce magnetic moment in graphene, hydrogen atoms and fluorine atoms are chemically absorbed on it and both methods are able to create an imbalance in the crystal lattice and induce a magnetic moment [6]. It is also promising to overcome this challenge by combining graphene with other 2d materials. The other challenge lies in extending spin lifetime, which is very important in applications. Theoretical prediction of this lifetime is around a microsecond. The huge difference between theory and experiment is still not explained. The most possible source is extrinsic origin, such as impurities, defects or ripples[7].

Another potential solution is to combine graphene with ferromagnetic (FM) material. For instance, in the graphene/Fe/Ni(111) system a magnetic moment is induced in the graphene layer, aligned parallel to the Ni 3d and Fe 3d magnetization[8]. Rougemaille et al. [9] found that graphene promotes perpendicular magnetic anisotropy in Co films in a graphene/Co/Ir(111) system where the graphene/Co interface has unusually strong contribu-

tion, exceeding that of most standard interfaces between Co and heavy metal layers. The similar system graphene/Co/Pt(111) has also been studied and the magnetic anisotropy was also found to be enhanced by the interaction between graphene and Co. This enhancement is explained by a conduction electron mediated Rashba-DMI (Dzyaloshinskii-Moriya interaction) mechanism. The interaction at the graphene/Co interface points opposite to the DMI induced by spin-orbit coupling at the Co/Pt interface, and results in a reduction of the total DMI of the stack [10, 11]. One advantage of these materials is that the graphene layer protects the ferromagnet from air oxidation.

To make a graphene/FM/substrate material, single layer graphene is firstly prepared by chemical vapor deposition (CVD) on the substrate. Ir(111) and Pt(111) are found to be more favorable as they allow single-layer graphene growth and also promote a perpendicular to-the-surface magnetization. Then Co or Fe thin films are evaporated on top of graphene by molecular beam epitaxy (MBE). After that, the Co or Fe atoms are intercalated between graphene and the substrate when the system is annealed. The annealing temperature is well controlled to avoid intermixing of Co and the substrate. However, the substrates often used, bulk single-crystal Ir(111) and Pt(111), are very expensive and so far limit the potential application of the graphene/FM/substrate system. More generally speaking, the cost of the substrate should be considered in all graphene CVD growth process. To reduce this cost, it is possible to replace the bulk single-crystal Pt(111) with an epitaxial high quality Pt(111) thin film prepared on a commercial substrate. Ajejas et al [10] prepared such hybrid system by using MgO(111) as the substrate and they found that MgO(111) does not influence the interaction between graphene and Co. During this internship, the possibility to use different kinds of substrates, especially silicon and sapphire, for the preparation of Pt(111) high quality thin film is explored. The structure of the thin film is characterized with the help of X-ray diffraction and their surface morphology is characterized by atomic force microscopy and X-ray reflectivity.

Part I

Scientific background

I.1 High quality thin film preparation

Preparing high quality thin film has long been an important subject in crystallography, especially with the development of integrated circuit fabrication. Several methods allows to grow high quality thin films on the substrates, and it is also possible to treat the thin films to ameliorate the quality after growth.

The growth of thin films can be classified into three modes. In the first mode, a film covers the substrate and thickens uniformly in the Frank-van der Merwe (FM) mode, which is also called the layer-by-layer mode. This mode is rarely observed. The more common mode is that the deposited material aggregates into three-dimensional clusters. In the Volmer-Weber (VW) growth mode, the clusters form directly on the bare substrate. In the Stranski-Krastanov (SK) growth mode, the clusters form on top of a very thin and uniform film of the deposit. SK happens when there are strong interactions between the film atoms and the substrate. Which mode is observed given the nature of the thin film and the substrate can be predicted according to the surface free energies. The FM mode is favored when the surface free energy of the substrate is big enough compared with the surface free energy of the thin film, and the VW mode is favored in the opposite case. The SK mode results from the differences between the thin film and bulk properties, so that the surface free energy varies as the thin film grows thicker. The deposition of thin films involves two steps. The first step is nucleation and the second is particle growth. In order to prepare high quality thin films, the nucleation density should be the lowest or the localization of nucleation should be controlled. Additionally, we want that the growth of the nuclei does not introduce defects and that the process is selective, towards a unique crystalline phase.

Chemical bath deposition (CBD) is an old deposition method. The principle of the CBD technique consists in the controlled generation of the metal and chalcogenide ions in an alkaline medium and their ion by ion deposition on the substrate in order to form a film. Research shows that this method is able to prepare high quality metal chalcogenide thin films that may be applied into large area photodiode arrays, solar selective coatings, solar cells, photoconductors, sensors and so on. Many deposition methods can be used to prepare such thin films, but CBD is favorable as it does not require expensive equipments and a large range of substrate can be used in the process. The deposition temperature is relatively low, which avoids oxidation and corrosion. The nucleation and grain growth are very sensitive. Many parameters can be controlled and adjust the quality of the thin film, such as temperature, growth duration, composition and pH of the solution and the nature of the substrate. The temperature is usually below 100°C and the deposition speed is about 1 μm/h. Glass is good enough as a

substrate for CBD, and it is also possible to use stainless steel and sapphire. The thin film obtained can be highly oriented. However, the roughness is about 10nm, which is not good enough for our research [12].

Molecular beam epitaxy (MBE) is a method that may grow single crystal thin films. Elements in ultra-pure form are heated in separate chambers until they begin to sublime or evaporate. The gaseous atoms then condense on the substrate (which can be a piece of wafer or a full wafer) and reaction between different elements is possible in this process. The evaporated elements do not interact with each other until they reach the wafer, due to the long free paths of these atoms in the high or ultrahigh vacuum chambers used during MBE. MBE allows the thin films to grow epitaxially. For instance, good quality Fe films were grown on GaAs [13]. The RHEED patterns in Fe(110), Fe(111) and Fe(001) directions showed characteristics of a flat oriented single crystal. The RHEED patterns also revealed that the corresponding Fe and GaAs crystal directions were aligned. Single crystal Fe thin films were grown epitaxially on GaAs.

As a subclass of chemical vapor deposition (CVD), atomic layer deposition (ALD) is a method to produce extremely thin and periodic atom layers. There are usually two chemicals, also called precursors in this process. The reaction chamber is under medium vacuum and some of the precursor I is pulsed into the chamber. The precursor I is bound to the substrate in a self-limiting manner because of chemisorption or surface reaction so that a single layer is formed. Then the chamber is purged and some of the precursor II is pulsed into the chamber. The precursor II reacts with the layer of precursor I still in a self-limiting way. By repeating this process, a repetitive thin film is obtained. The thin film is not necessarily of high quality, sometimes even amorphous. However, plasma enhanced ALD is able to produce high quality nitride and oxide films. High quality Al₂O₃ films are formed in this way. After the Al precursor pulse, the reaction chamber is injected with H₂ plasma. Then the Al layer is oxidized with O₂ plasma. Al₂O₃ films with the thickness of 15 nm are grown in this way and showed very good electrical properties [14].

Another subclass of CVD, metalorganic chemical vapour deposition (MOCVD), is used to prepare single or polycrystalline thin films by chemical reaction. Ultra pure gases are introduced into a reactor. These gases are the precursors, and at least one of the precursors is organic. The organic precursor molecules decompose in the absence of oxygen when heated in the chamber. The more carbon atoms are attached to the central metal atom, the weaker the bond is. Atoms of the required element are deposited on the substrate surface with which they form bonds. In this way an epitaxial layer is grown. High quality GaAs layers were grown on Si substrates by MOCVD [15]. The layers were proved to have single domain structure, mirror-like surface, high electron mobility, fairly high photoluminescence intensity and low etch pit density.

Another method that can be used to produce high quality thin film is the pulsed laser deposition. The material to be deposited is prepared in the form of a target which is vaporized by a pulsed laser beam. This process involves the formation of a plasma plume between the substrate and the target. When the plasma hits the substrate a thin film is deposited. It is possible to feed gas into the reaction chamber so that the plasma reacts with the gas and produces some specific thin films. Suda et al. [16] prepared several TiO_{2-x}N_x samples by controlling the nitrogen/oxygen gas mixture composition fed into the chamber. AFM measurement showed that the thin films prepared had a roughness lower than 10 nm. The crystalline structure was found to be oriented and its composition to depend on the nitrogen concentration ratio. However, XRD measurements showed that the crystal lattice size was relatively small.

What we want to use in our experiments, sputtering deposition is a relatively fast growth method. The principle of this method is presented in the next part of this paper. One advantage of this deposition method is that the roughness of the thin film can be very low. The thickness of the deposited film can be very homogeneous, with a roughness that can be about 1 nm as long as the roughness of the substrate is low enough [17]. However, the crystal lattice of the thin film can be smaller than the bulk value due to some porosity. It is possible to ameliorate the structure of the thin film by heat treatment, during the deposition or after the deposition.

Hu et al. [17] prepared indium tin oxide (ITO) films on glass substrates by rf (radio frequency) magnetron sputtering. The substrates were annealed in air or in vacuum at different temperatures and then thin films of ITO were deposited onto the substrates. According to AFM measurement, the roughness of the surface was 1-2 nm. The higher the deposition temperature, the rougher the surface. The surface images showed that when the deposition temperature was higher, the grain on the surface was bigger and more uniform. The films annealed in air were rougher than those annealed in vacuum. XRD measurements showed that the films deposited below 300°C were amorphous and highly oriented when the substrate temperature was higher than 400°C. The optical and electrical properties were also improved at higher temperature in vacuum. The growth of poly-crystal zinc oxide (ZnO) films by rf magnetron sputtering gave similar results [18]. The thin films prepared at higher temperature were rougher and the grains were larger. In both cases, thin films prepared at higher temperature had more uniform crystalline structure and were better oriented. The reason for this phenomena is that high substrate temperature enhances the mobility of surface adatoms, which leads to low nucleation density and forms an optimal crystalline atomic configuration.

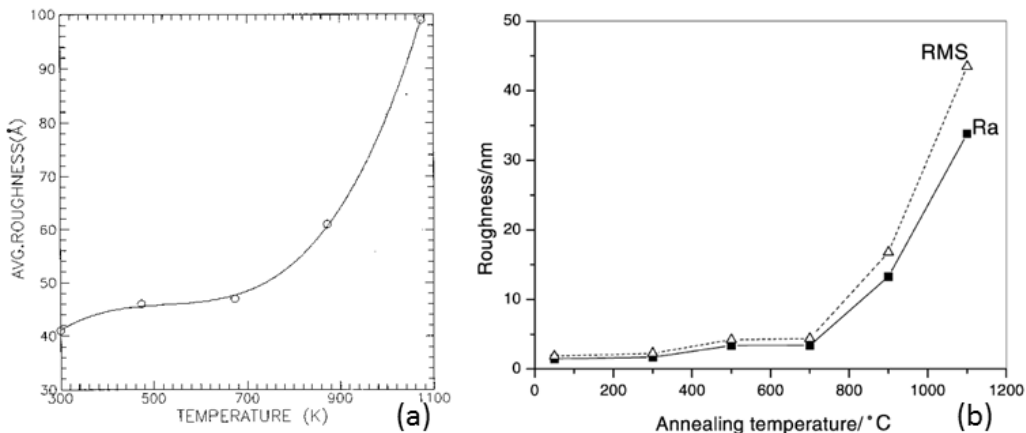


Figure I.1: Roughness of (a) ZnO and (b) TiO₂ thin films after annealed at different temperatures. The sudden change in the roughness of ZnO is at about 673K and the sudden change of TiO₂ is at about 700K

It is also possible to anneal the as-deposited thin films. The annealing of ZnO thin films has been studied. Similar to the results mentioned above, the crystallinity was improved, the grain size and the surface roughness were increased. It was remarkable that the roughness stayed stable and the crystal structure did not change much when the annealing temperature was below 673K. There was a sudden change at 673K and the roughness was increased above this temperature (Fig.I.1 (a)). It has been observed that above 673K, coalescence occurred which caused major grain growth leading to microcrack formation and surface roughness augmentation [19]. Another study [20] focusing on both the annealing temperature and

ambient condition leads to similar conclusion in terms of crystallinity and roughness. XRD measurement also showed a deviation of the peak position. The deviation compared with the standard structure was smaller when the annealing temperature was higher. This meant that the residual stress was eliminated by annealing. Hou et al. did similar studies on titanium oxide (TiO₂) thin films. The as-deposited thin films were amorphous. When the thin films were annealed, TiO₂ was more oriented. In XRD pattern, when the annealing temperature increased some peaks appeared and became narrower. The roughness also increased as the temperature augmented. Similar to ZnO, the structure of TiO₂ kept stable below 700°C and a sudden change occurred above 700°C (Fig.I.1 (b)). Thermal annealing of GaAs layers showed that annealing can also be used to reduce the density of defects [21].

The orientation of the thin films depends on the orientation of substrate. Epitaxial Pt(111) thin films can be grown on MgO(111) and Al₂O₃(0001) [22]. What we want to know is the structure of Pt thin films prepared on the substrates by sputtering deposition and how it evolves at high temperature.

I.2 Large area CVD growth of graphene

There is continuous effort in developing and optimizing methods to prepare high quality single layer graphene. Chemical vapor deposition (CVD) on transition metal is proved to be an efficient method. For instance, some experiments were done on Ni, and the graphene could not be perfectly single layer due to the relatively high solubility of carbon in Ni. This problem was partially solved by using metals in which carbon solubility was lower, such as Cu [23]. The quality of graphene depends on the quality of the substrate. Continuous graphene sheet with single crystallographic orientation was obtained by using high quality thin film of Co [24], Ru [25], Ni [26] and Cu [27]. Ir and Pt are also good substrates due to their low C solubility that limits the growth to single layer. The interfacial interaction between graphene and Ni(111) and Ru(0001) is strong while it is much weaker for Cu, Pt and Ir. The weak interaction may be preferred because it will be easier to exfoliate the graphene sheet. CVD can be done under ultrahigh vacuum (UHV). It is also possible to do the deposition close to or at atmospheric pressure, for example, in a CVD reactor using thin films and metal foils as substrates [28].

The mechanism of graphene CVD with hydrocarbons, such as CH₄, can be described with the following steps : (i) adsorption of CH₄ on substrate surface ; (ii) partial dehydrogenation of CH₄, leading to C species such as CH_x (x = 1,2 or 3) ; (iii) surface diffusion of C species on the surface ; (iv) C species nucleation on the active sites of the substrate to form graphene domains ; (v) growth of graphene domains by incorporation of C species at their edges ; (vi) coalescence of adjacent graphene domains to form polycrystalline graphene films. In order to have a monocrystal graphene, the key point is to decrease the graphene nucleation density so that as few as possible, preferably only one crystal would grow.

Pt is often used for graphene CVD growth. Pt has low C solubility in the bulk so single layers can be prepared. The interaction between the graphene layer and the Pt surface is one of the weakest among transition metals, similar to graphene on Ir(111). Pt(111) was used by Sutter et al. to grow single layer graphene [29]. A Pt(111) single crystal was exposed to ethylene at above 1000°C. A mono-layer graphene was prepared and characterized with LEEM (low-energy electron microscopy), LEED (low-energy electron diffraction) and micro-ARPES (angle resolved photoemission spectroscopy). At high temperature, graphene nucleation was observed and adjacent nuclei were separated by typically 100 μm. In fact, upon exposure at high temperature to ethylene, carbon dissolved in the bulk. Slowly decreasing the temperature led to surface segregation of C, from which graphene grew. After the appearance of the

nuclei, each graphene domain rapidly expanded by attachment of C to the edges to reach a size of several tens of micrometers in around 1 min. The growth by edge attachment was a continuous process and no secondary nucleation was observed. As a result, single-crystalline graphene domains were formed on Pt(111) crystal. The evolution of step edges is shown in Fig.I.2 (e). The direction in which the step edges grew the slowest was defined as uphill and the direction in which the growth was fastest was defined as downhill. The growth velocity in the uphill and downhill directions in a graphene domain was measured. They differed by about a factor of 2 and both decreased slowly at constant temperature, following an exponential dependence with time constant $\tau=280$ s. This characteristic time represented the decrease in the density of surface carbon owing to the depletion of the reservoir of interstitial carbon in the metal substrate.

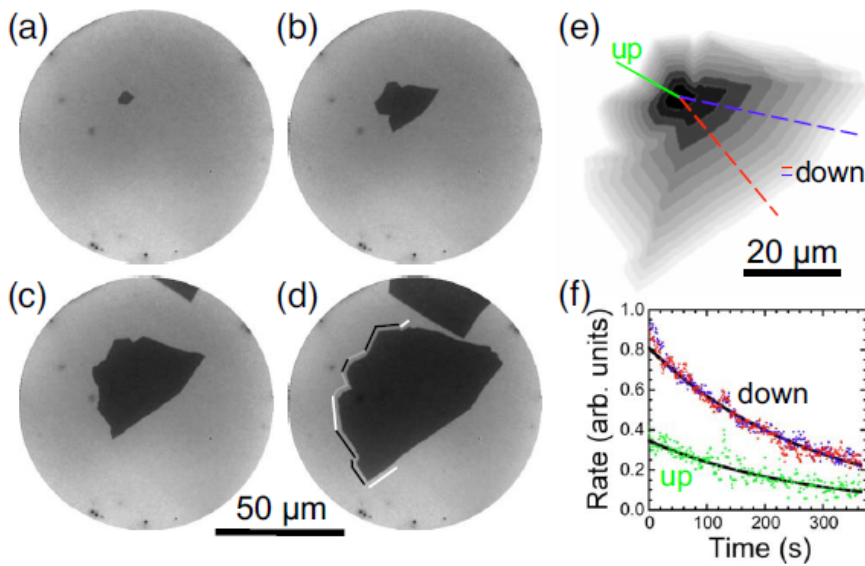


Figure I.2: Mono-layer graphene growth on Pt(111). [(a)–(d)] Sequence of LEEM images obtained during growth of a single-crystalline ML graphene domain by carbon surface segregation at constant $T=864$ °C. (e) Domain edge contours at constant time intervals of 6 s, illustrating the growth rates in different in-plane directions aligned with the uphill and downhill directions of the stepped substrate. (f) Graphene growth rates along the lines shown in (e). Solid lines are exponential dependent, with a universal decay time $\tau = 280$ s for all curves.

The mismatch in thermal-expansion coefficients between Pt ($8.8 \times 10^{-6} K^{-1}$) and graphene ($< 1 \times 10^{-6} K^{-1}$) caused a progressive buildup of compressive stress in the graphene layer when the sample was cooled down after growth. This stress was relaxed elastically by the formation of wrinkles but not by crystal defects in the graphene. Generally one set of wrinkles aligned with the predominant direction of the atomic steps of the substrate and followed a substrate step over micrometer distances. Although some deviations from the predominant directions existed, no clear correlation between the wrinkle direction and the six-fold symmetry of the substrate or graphene lattices was observed. A measurement of the time-dependent extension of the wrinkle showed that the propagation was not continuous but occurs in bursts, interrupted by extended periods without any measurable movement. The propagation of wrinkles in the graphene layer is actually a general phenomenon. It is not clear if the wrinkles still exist when the graphene sheet is exfoliated or transferred to another substrate, but this phenomenon should be controlled to acquire better surface morphology.

In order to determine the epitaxial relationship motifs between mono-layer graphene and the Pt(111) substrate, micro-diffraction was used to characterize single graphene domains (Fig.I.3). Some other studies pointed out that rotational disorder existed owing to graphene nuclei bonding to the metal substrate in a range of possible moiré structures [30]. The disorder can be observed in particular for weakly coupled systems, as the energy landscape is shallow and none of the possible coincidence structures lead to a clear global minimum in energy. According to micro-LEED patterns of single graphene domain, two different families of interfacial structures were observed. In large graphene domains with sizes exceeding 50 μm , $(3\times 3)_G$, $(\sqrt{6}\times \sqrt{6})R2_G$ and $(2\times 2)R4_G$ structures were found. On the other hand, smaller graphene nuclei ($10\mu\text{m}$) grown at the same time formed a range of large unit-cell coincidence structures, such as $(\sqrt{44}\times \sqrt{44})R15_G$, $(\sqrt{52}\times \sqrt{52})R14_G$ and $(8\times 8)_G$. *In situ* LEEM movies of the growth process revealed that both types of structures nucleated simultaneously and no significant difference in nucleation rate of graphene domains with different interfacial alignment was found. However, the large and small-cell moirés had different growth rates, which meant that kinetic factors might be the reason of the faster growth of the domains with small moiré unit cells. In general, the existence of well-defined moiré coincidence structures with non-vanishing lattice mismatches proves that the interaction between graphene and substrate is strong enough and creates a variety of epitaxial relationship. Similar moiré varieties occurred also on graphene grown on Ir(111) [31].

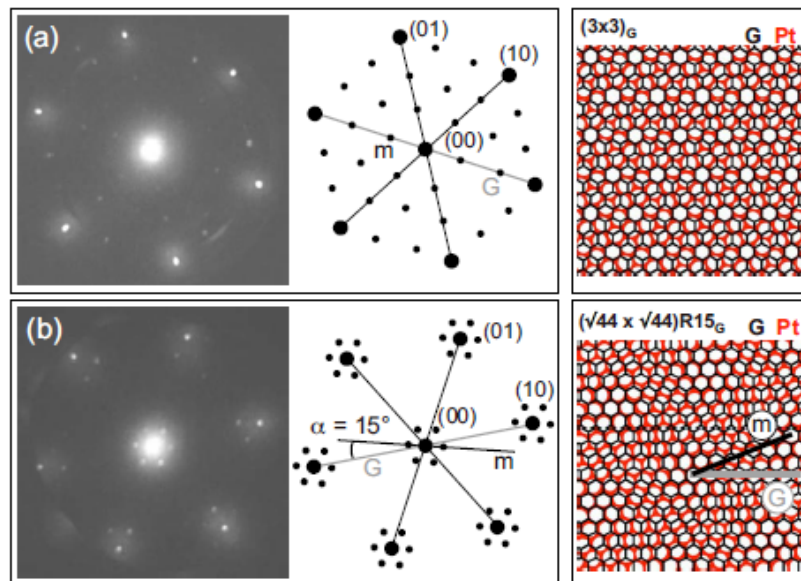


Figure I.3: Single-domain micro-LEED patterns of mono-layer graphene on Pt(111). (a) Graphene/Pt(111) moiré with $(3\times 3)_G$ periodicity relative to the graphene lattice. (b) Moiré structure with $(\sqrt{44}\times \sqrt{44})R15_G$ unit cell, relative to graphene.

The interface between graphene and substrate was characterized by intensity-voltage measurements in reciprocal space (IV LEED) or in real space (IV LEEM) and the distance between carbon atoms and Pt atoms could be calculated by simulation. To limit the computational complexity, the simulations were performed for a commensurate structure with a small unit cell and the only variable parameter was the graphene/Pt(111) interlayer spacing. According to the simulation result, the separation was $3.30 \pm 0.05 \text{ \AA}$, which was very close to the interlayer spacing in graphite (3.36 \AA). We could deduce that the coupling between graphene and metal was similar to a pure van der Waals interaction. A purely theoretical calculation based

on density functional theory (DFT) predicted that the distance is 3.30 \AA [32], which was in perfect agreement with the simulation on experimental result. The interface was simple and lied close to the c-axis spacing in graphite. Micro-ARPES maps of the band structure also proved the weak coupling. The map also shows that apart from some residual hole resulted from charge transfer with the substrate, the electronic structure of mono-layer graphene on Pt(111) was close to that of isolated graphene. The linear dispersion of bands in Dirac cones was also preserved, which leads to many exotic manifestations of massless Dirac fermions.

The remaining question is which parameters are optimal in graphene CVD growth, especially the temperature. Gao et al. [33] made a set of comparisons between 773K and 1073K. The graphene layer was characterized with STM and LEED. The domain boundaries and defects resulting from the nuclei of graphene domains were the bright spots in STM images (Fig.I.4). According to these images, graphene grown in ethylene at 773K had bigger domain size (Fig.I.4 (b)) than at higher temperature (Fig.I.4 (a)). The domain size for 1073K was very small (several to tens of nanometers) and the density of defects on the domain was very high. As is explained above, bigger domain size means low graphene nucleation density. Therefore the best temperature for high quality graphene CVD growth is about 800K. LEED patterns of graphene layer on Pt(111) substrate gave some information about the moiré structures. Three kinds of main rotation angles, 0° , 19° and 30° were detected, and the moiré patterns could be calculated by considering the rotation. According to previous research, supersonic methane molecules with a higher kinetic energy could induce highly oriented monolayer graphene [34]. However, according to LEED pattern graphene grown at different temperature was not highly oriented since all kinds of moiré structures existed for no matter the temperature.

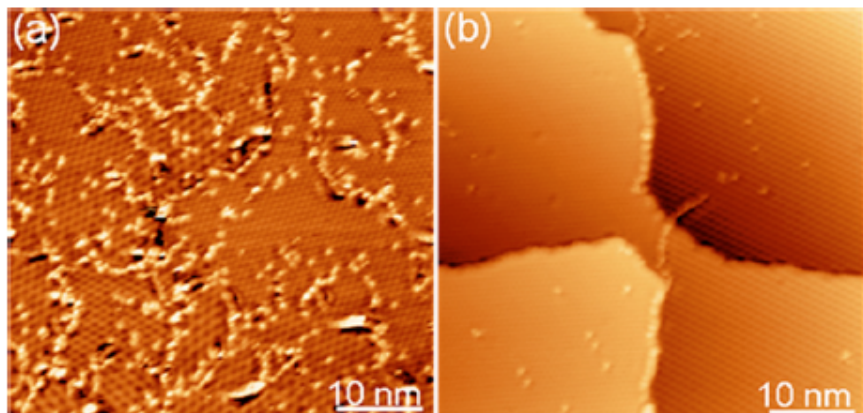


Figure I.4: STM images of graphene grown on Pt(111). (a) Grown at 1073 K, the domain size is small (several to tens of nanometers); (b) Grown at 773 K, the domain size is much bigger.

In our experiments, the graphene layer is meant to be used for Co intercalation. Defects are needed in this process, so the graphene we prepare should not be of the best quality. We can choose the temperature either lower than 800K or higher than 800K. 700K is chosen for graphene CVD growth.

Part II

Experimental techniques

II.1 Sputtering deposition

Sputtering deposition is a physical vapor deposition (PVD) technique to deposit thin film. What is used in our experiments is one of the most cost effective way of sputtering deposition, DC or direct current sputtering.

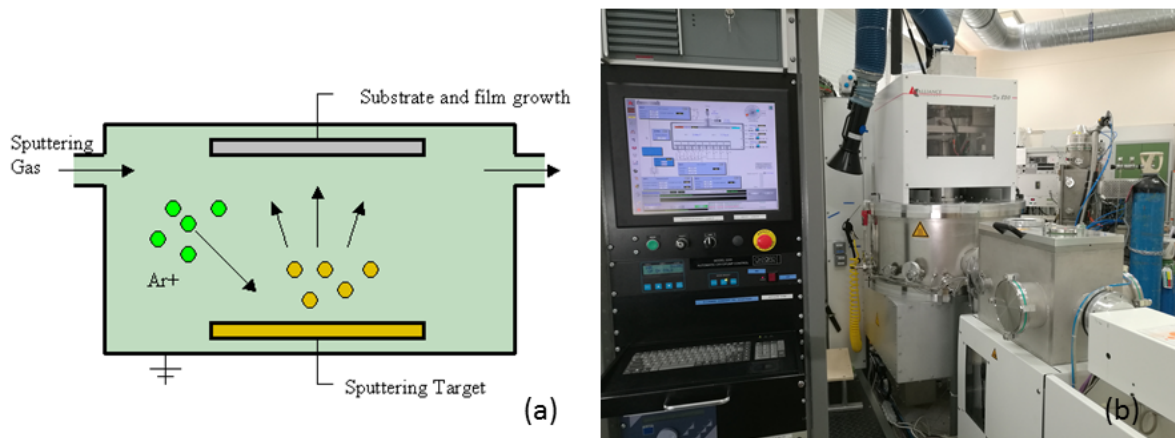


Figure II.1: (a) Principle of DC sputtering. There is a toroidal magnetic field under the sputtering target. The sputtering target is used as the cathode while the substrate is used as the anode. (b) The sputtering device used in our experiments.

A sputtering target and a substrate are put in the sputtering chamber. The sputtering target is connected with cathode and the substrate is connected with anode. The chamber is in high vacuum and low concentration of sputter gas, argon in most cases, is injected into the chamber. A high voltage is applied between the anode and the cathode so that argon atoms are ionized. Argon cations bombard the sputtering target because of the electric field. Some particles escape from the sputtering target during the bombardment and the majority of them are neutral, i.e., Pt atoms in our experiments. The atoms are deposited onto the substrate when they hit it (Fig.II.1 (a)). If the concentration of argon is too high, a high flux of Pt atoms would collide with argon atoms and slow down the deposition, but in general the deposition speed of DC sputtering is relatively fast compared with other methods. On the other hand, according to Paschen's law too few argon atoms will be ionized if the concentration of argon is too low. Besides the sputter gas concentration there are some other controllable parameters

that help the operator to control the growth and micro-structure of the thin film, such as the temperature of substrate.

Compared with evaporation deposition, sputtering deposition provides much more energy to the target atoms. Higher energy helps atoms bond to the substrate surface, form some special texture and increase surface diffusion.

There are other methods of sputtering deposition. For example, in DC sputtering ions accumulate on the substrate and might cause problems. RF, or radio frequency sputtering can avoid this problem by using alternative current instead of direct current, but it is more expensive. In our experiments the charge does not cause problems and we want to explore a cost effective way of preparation, so DC sputtering is applied.

II.2 AFM

Atomic force microscope (AFM) is used to characterize the surface of the sample. A cantilever with a tip is fixed on a support and can move in xyz directions with the use of a piezoelectric drive. The support can move in the z direction and the sample can move in the xy direction. A laser beam reflects on the tip and is detected by a camera. The camera is made of many photodiodes so that the movement of the tip is precisely measured. When the tip is close enough to sample, it is possible to measure the force between the atoms of the tip and the atoms on the surface of the sample. The forces can be classified into attractive and repulsive forces. For attractive forces, van der Waals interaction, electrostatic force and chemical force are included. The repulsive forces can be considered as hard sphere repulsion, Pauli-exclusion interaction and Coulomb interaction.

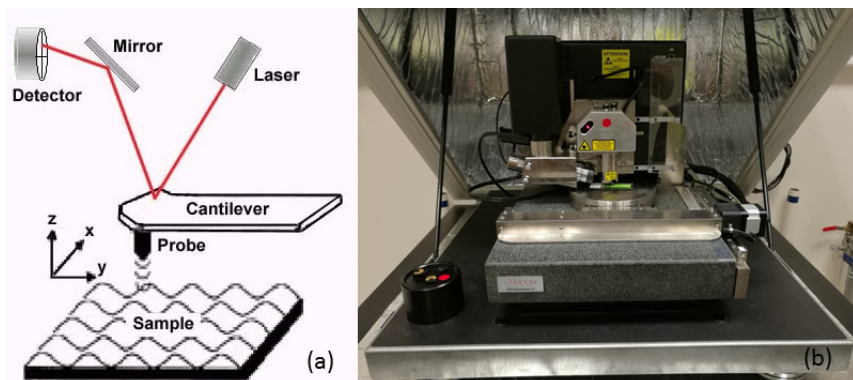


Figure II.2: (a) Mechanism of AFM. (b) The AFM used in our experiments.

In our experiments, the AFM works in tapping mode. In this mode, the cantilever is driven to oscillate up and down at or near its resonance frequency and AFM does amplitude modulation. The frequency is fixed. The interaction between the tip and the sample is approximated as the Lennard-Jones potential. This potential is a simple model that approximates the interaction between a pair of neutral atoms or molecules. The potential has an attractive regime and a repulsive regime, repulsive in short-range and attractive in long-range. The tip stays at a constant height and the amplitude is reduced differently at every point of the sampling area. From the amplitude we can calculate the force, and from the force we can calculate the distance between the tip and the sample surface according to Lennard-Jones potential. In the end AFM measurement is able to create an image of the sample surface.

Compared with other microscope like SEM, AFM gives a three-dimensional image of the surface instead of a two-dimensional one. It can work in ambient conditions. There is no need for special treatments and the sample is not likely to be damaged, especially in tapping mode.

II.3 XRD and XRR

X-ray wavelengths are in the range of 0.001-10 nm. This is close to the distance between atoms in crystals and molecules. Therefore, X-ray can be used to study the molecular and atomic structures. The interaction between X-ray and a single molecule is too weak to be detected, so only a large number of molecules or atoms can be studied by using X-ray. X-ray crystallography is widely used to characterize crystal structures. In our experiments, the X-rays are used for X-ray diffraction and X-ray reflectivity experiments.

In X-ray diffraction, X-ray waves are scattered elastically by the electron cloud of the atom. These waves have destructive interferences in most directions while interfere constructively in a few specific orientations according to Bragg's law (Fig.II.2 (a)):

$$2d\sin\theta = n\lambda$$

where λ is the X-ray wavelength, θ is the scattering angle, n is an integer number called diffraction order, and d is the distance between crystallographic planes.

According to Bragg's law, the distance between atomic layers can be calculated. As this distance is specific for each crystalline structure, we can identify the nature of the sample according to the diffraction pattern. The relative intensity of all the peaks is used to deduce the crystal motif. The FWHM, or full width at half maximum is used to estimate the crystallite size according to Debye-Scherrer equation. However, the broadening of the peak may be caused as well by instrumental reasons, microstrain, solid solution inhomogeneity and other factors. As a result, the calculation of the crystallite size is often a rough estimation.

The X-ray diffractometer that we use is specially designed for thin film characterization and works in different modes. X-ray symmetrical diffraction measures the diffraction between the atom layers parallel to the surface. The detector is at the symmetrical position of the X-ray source with respect to the surface. The incident angle is relatively large and the incident ray usually penetrates the thin film deeply and gives some information about the atom layers of the substrate, too. By combining the symmetrical diffraction with a rotation of the sample around an axis, we can get the pole figure of the crystal lattice in the thin film.

X-ray grazing incidence diffraction gives more information about the surface of the thin film. The incident angle is very small, just a little bigger than the critical angle so that the X-ray beam does not reach the substrate. The X-ray source is fixed and the detector does an out-of-plane scan. From the diffraction pattern we can know which atom layers exist on the surface and deduce the structure of the surface.

Diffraction between atom layers involves a scattering vector $\vec{Q} = \vec{k}_f - \vec{k}_i$, having a modulus comparable to the reciprocal lattice vectors. When $\|\vec{Q}\|$ is much smaller, other characteristic lengths can be probed, for instance the thickness of the thin film. To probe this, the symmetrical geometry can be used with small incident and reflected angles, to perform an XRR, X-ray reflectivity experiment. In such experiment we actually probe interferences between waves reflected at the surface and at the buried thin film/substrate interface. The intensity of the reflected beam is very weak except for the beam with a very small incident angle, close to the critical angle. Critical angle is the onset angle for total reflection and for X-ray reflection it depends on the electronic density of the surface. When the incident angle is larger than the

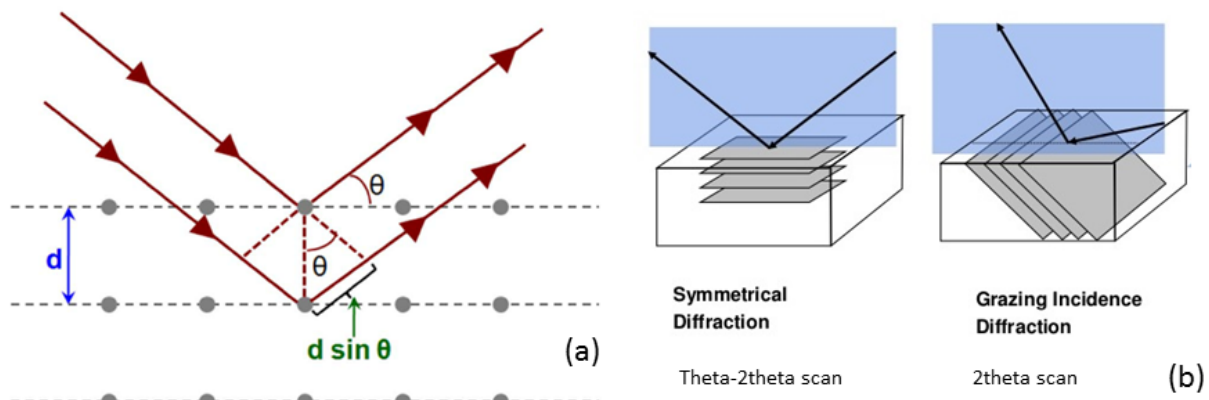


Figure II.3: (a) Mechanism of Bragg's law. (b) Geometry in the two modes of XRD that we use: symmetrical diffraction and grazing incidence diffraction.

critical angle, the intensity of the reflected beam decreases and the gradient depends on the roughness. The rougher the surface and the interfaces are, the more X-ray is scattered and not reflected. According to Snell's law, the optical path length of the waves reflected by the interfaces can be calculated with the indices of refraction. When the optical path difference equals to integer multiple of wavelength, the interference between waves scattered by the surface and by the interface results in an intensity maximum. X-ray reflectivity by thin films shows oscillations versus scattering angle, and the period of these oscillations, according to the Bragg's law, depends on the thickness of the thin film (Fig.II.4). XRR and AFM give very complementary information about the roughness : XRR gives access to buried interfaces, and AFM gives estimates of the roughness with no need for modeling and particular assumption on the nature of the roughness [35].

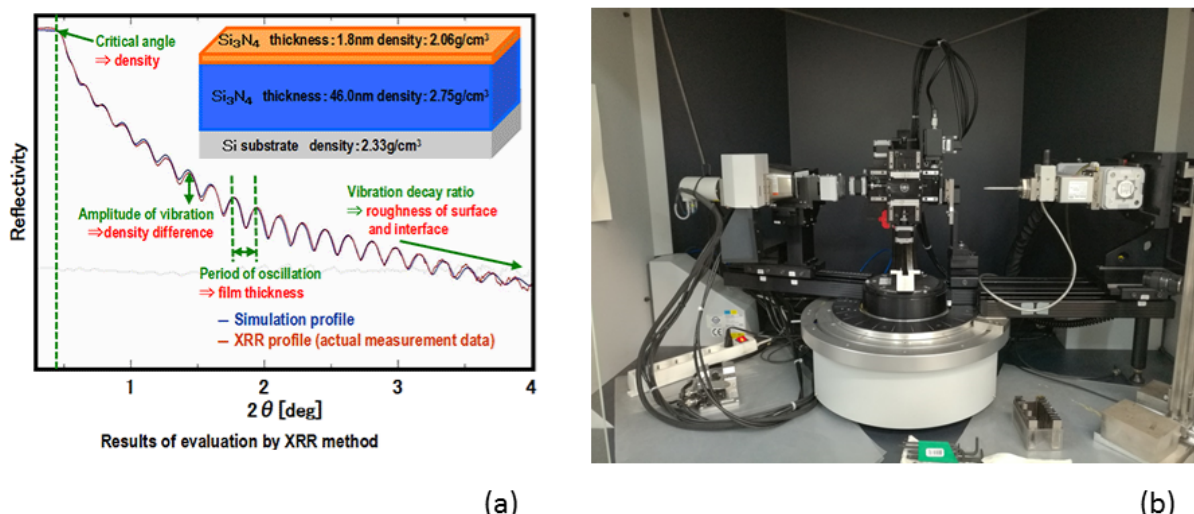


Figure II.4: (a) A typical XRR pattern. Electronic density, roughness and thickness can be acquired by simulation and curve fitting. (b) The X-ray diffractometer used in our experiments.

II.4 Experiment process

Commercially available MgO(111), Al₂O₃(0001), SiO₂(2 nm)(001)/Si and SiO₂(300 nm)(001)/Si are used as substrates. We note the SiO₂(2 nm)/Si substrate as Si and the SiO₂(300 nm)/Si as SiO₂. They are cleaned with ultrasonic and acetone, and then dried in argon. The surface of the substrates are first characterized with AFM. The roughness of an area is defined by Rq, the root mean square deviation in z direction. The roughness of a sample is evaluated by taking the average Rq of five sampling areas on the surface. In most cases, our sample is rectangular and the sampling areas are chosen by quartering the length and the width.

Then these substrates are put into the sputtering chamber. The sputtering process consists of three steps. The first step is pumping. In this step the samples are attached to a Cu plate and the plate is put into the sputtering chamber. The pressure in the chamber decreases to 5×10^{-7} mbar. The second step is pre-sputtering which takes 30 s. In this step 45 sccm of Ar is introduced into the chamber. The sputtering target is bombarded by argon cations but the substrate is not exposed to the sputtered atoms, so that the sputtering target is cleaned in vacuum. The last step is sputtering. In this step, the distance between the substrate and the sputtering target is 100 mm and a large voltage is applied between them so that the power of sputtering is 20 W. We control this step either by choosing the sputtering power or by choosing the sputtering voltage, and only one parameter is known in the control program. The pressure in the chamber is 5×10^{-7} mbar and 20 sccm of Ar is introduced into the chamber. The deposition rate is estimated to be about 0.15 nm/s and the sputtering step lasts for 65 s to get a 10 nm Pt thin film on the substrate. At last the sample is put out of the sputtering chamber and the pressure in the sample chamber is increased until we can put the sample out.

Then the samples are characterized with AFM, XRR and XRD. All X-ray measurements are operated on the same X-ray diffractometer. X-ray beams are emitted from a Cu anode and the wavelength is 0.15418 nm. Finally Pt/Si and Pt/Al₂O₃ samples are annealed at 700K in a ultra-high vacuum chamber for 30 min. After that these two samples are characterized by AFM, XRR and XRD again.

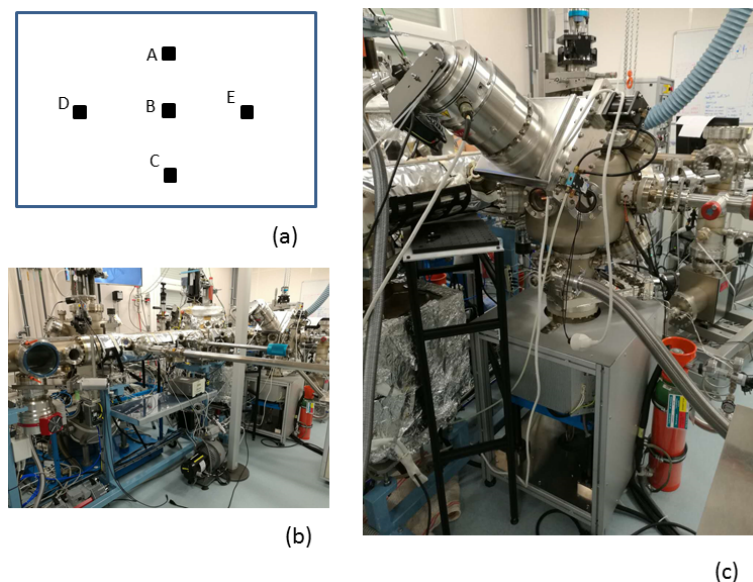


Figure II.5: (a) For each sample, five sampling areas are chosen by quartering the length and width of the surface. (b) The ultra-high vacuum device used in our experiments. (c) The annealing chamber of the device.

Part III

Results and discussion

III.1 Morphology of deposits

Four substrates are used in our experiments : MgO(111), Al₂O₃(0001), SiO₂(2 nm)(001)/Si and SiO₂(300 nm)(001)/Si. We note the SiO₂(2 nm)/Si substrate as Si and the SiO₂(300 nm)/Si as SiO₂. As is mentioned before, the roughness of an area is defined by Rq, the root mean square deviation on z direction. Roughness of the sample is the average Rq of five sampling areas on the surface. These sampling areas are chosen by quartering the length and the width of the surface. The standard deviation of roughness between these areas is the uncertainty. If the calculated uncertainty is smaller than 0.01 nm, we take 0.01 nm as the uncertainty considering that AFM is not able to measure below this scale.

The roughness of these substrates are measured with AFM before any treatment. The roughness of Si and SiO₂ wafers is very small. The roughness of Si is 0.15 ± 0.04 nm and that of SiO₂ is 0.17 ± 0.03 nm. The Al₂O₃ substrate is very flat, too and its roughness is 0.3 ± 0.1 nm. The roughness of MgO substrate is much larger, i.e. 1.9 ± 0.3 nm. The sampling areas are $1 \mu\text{m} \times 1 \mu\text{m}$, but we also take an image of a bigger scale to know if there is some large scale structure. Nothing special is found for Si, SiO₂ and Al₂O₃, but for MgO, linear traces are observed on the surface of this substrate and the height difference is about 5 nm (Fig.III.1 (d)). A height profile of the red line on MgO surface is shown in Fig.III.1 (f), where we can see the height of a trace is 5 nm lower than the surface. Traces on MgO may be formed during preparation process.

Substrate	Si	SiO ₂	MgO	Al ₂ O ₃
Before deposition	0.15	0.17	1.9	0.3
As-deposited	0.12	0.13	1.9	0.3
Annealed	3.7	-	-	0.40

Table III.1: Roughness (rms) of the samples in different status (nm)

The roughness after sputtering deposition does not change much (Fig.III.2). The roughness of the samples are : Pt/Si, 0.12 ± 0.02 nm; Pt/SiO₂, 0.13 ± 0.04 nm; Pt/Al₂O₃, 0.3 ± 0.1 nm; Pt/MgO, 1.9 ± 0.3 nm. We can deduce that the Pt thin films prepared with sputtering deposition are very homogeneous on the substrates. We also take an image of a bigger scale. Nothing special compared with small scale is found on the surface of Pt/Si, Pt/SiO₂ and Pt/Al₂O₃. Still on Pt/MgO the linear traces are visible. The surface of Pt/MgO sample is a little different from the substrate. Plateaus and valleys are found in both big scale image (Fig.III.2 (d)) and small scale image (Fig.III.2 (c)). A height profile of the red line in Fig.III.2

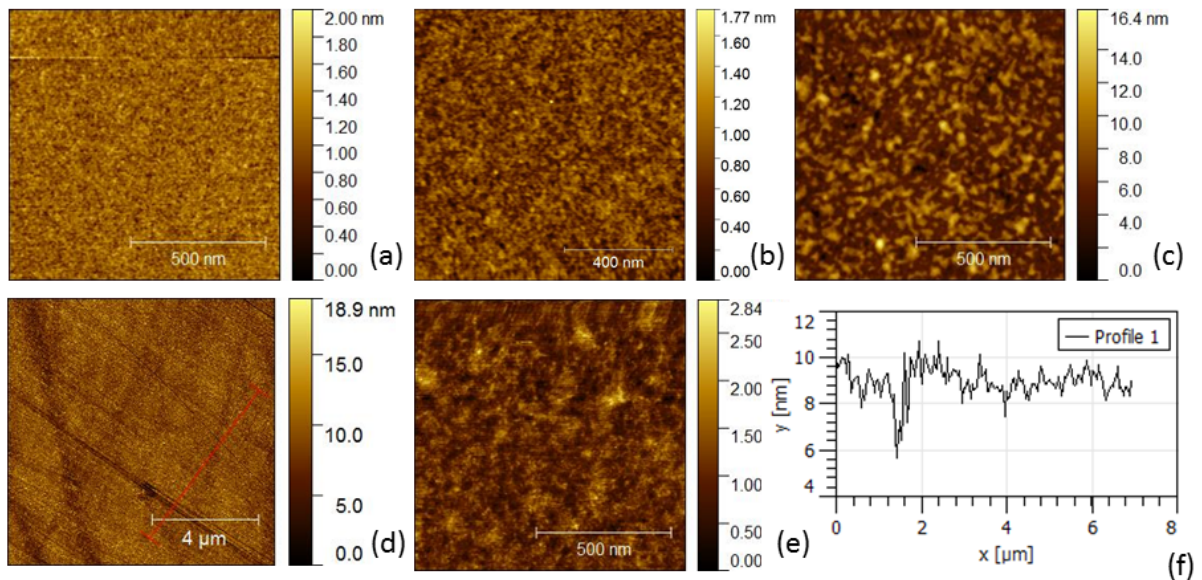


Figure III.1: AFM images of the commercially available substrates before any treatment : (a) Si, $1 \mu\text{m} \times 1 \mu\text{m}$ (b) SiO₂, $1 \mu\text{m} \times 1 \mu\text{m}$ (c) MgO, $1 \mu\text{m} \times 1 \mu\text{m}$ (d) MgO, $10 \mu\text{m} \times 10 \mu\text{m}$, linear traces are observed (e) Al₂O₃, $1 \mu\text{m} \times 1 \mu\text{m}$ (f) A height profile of the red line in image (d) and a trace is shown

(d) is shown in Fig.III.2 (f). In this height profile we can see three traces whose height difference is still about 5 nm.

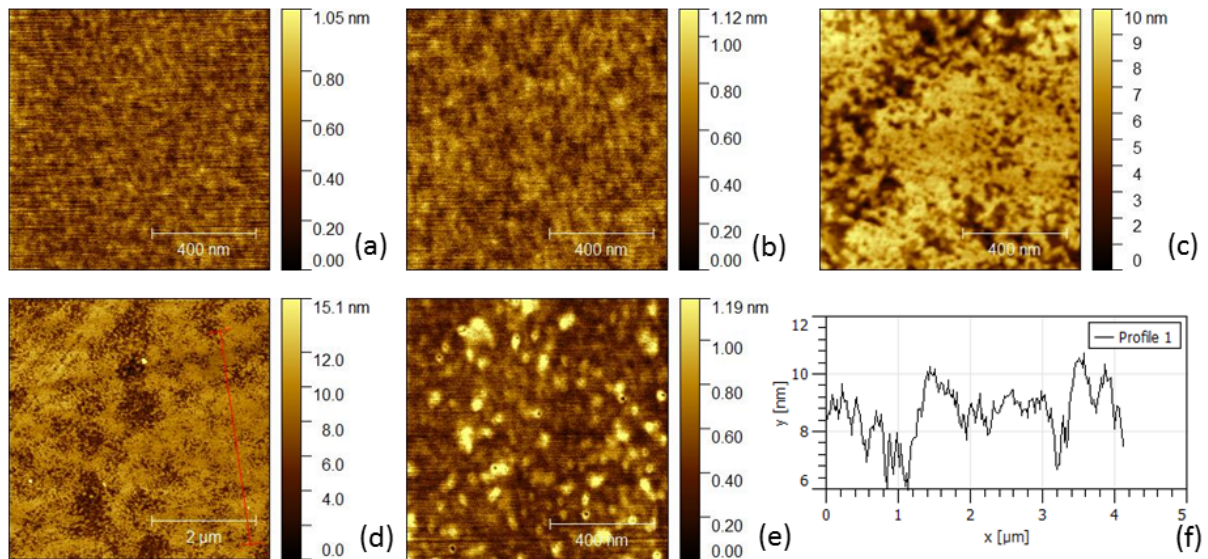


Figure III.2: AFM images of as-deposited samples after the deposition of 10 nm of Pt : (a) Pt/Si, $1 \mu\text{m} \times 1 \mu\text{m}$ (b) Pt/SiO₂, $1 \mu\text{m} \times 1 \mu\text{m}$ (c) Pt/MgO, $1 \mu\text{m} \times 1 \mu\text{m}$ (d) Pt/MgO, $5 \mu\text{m} \times 5 \mu\text{m}$ (e) Pt/Al₂O₃, $1 \mu\text{m} \times 1 \mu\text{m}$ (f) A height profile of the red line in image (d) and three traces are shown

XRR measurement results of Pt/Si, Pt/SiO₂, Pt/MgO and Pt/Al₂O₃ after deposition are respectively shown in Fig.III.3. In each image, the black curve is the measurement result. The fitting range is between the blue vertical line and the red vertical line. The blue line is a local maximum which corresponds to the critical angle of total reflection. The red line is a point

PART III. RESULTS AND DISCUSSION

on the oscillation and it is preferable to place the red line at a local minimum as far from the blue line as possible. Then a fitting curve is calculated by genetic algorithm according to the measurement result in the fitting range, which is the red curve in the figures. The calculation is based on Parratt formalism, a theory used to predict the reflectivity of a system with several interfaces. The position of the maximum is used to calculate the electronic density, and, since we already know the density of Pt, the maximum can be used to calculate the mass density of Pt thin films. The uncertainty of density is $\pm 0.1 \text{ g/cm}^3$. The slope of the curve informs on the roughness. The uncertainty of roughness is $\pm 0.1 \text{ nm}$. The period of oscillation reveals the thickness of the thin film. The uncertainty of thickness is $\pm 0.1 \text{ nm}$. As we can see, the curve of Pt/SiO₂ can be perfectly fitted, which means that the thin film is very consistent with the model of Parratt formalism. The oscillations of Pt/MgO vanish for smaller angle than the other patterns and the slope of Pt/MgO is larger. This means that the surface is rougher, which is consistent with the AFM measurement results. The amplitude of oscillation for Pt/MgO and Pt/Al₂O₃ is smaller compared with Pt/Si and Pt/SiO₂. The amplitude depends on the roughness and the density difference between the thin film and the substrate. It is true that the density of MgO (3.6 g/cm³) and Al₂O₃ (3.6 g/cm³) are closer to that of Pt than Si (2.3 g/cm³) and SiO₂ (2.7 g/cm³).

According to the XRR measurement results (Table III.2), the roughnesses of the Pt surface and the Pt/substrate interface are almost the same. This confirms that the thin film prepared by sputtering deposition is very homogeneous. The roughness of the sample Pt/MgO is different from that measured by AFM. The roughness calculation based on Parratt formalism supposes that the height distribution function of the surface is Gaussian, and this is especially not true for the sample Pt/MgO as the traces are very steep. AFM does no supposition on the surface relief [35]. Therefore, the roughness measured by these two devices can be different and the result of AFM is more credible. However, qualitatively the XRR results also show that the Pt/MgO is rougher. As for the thickness, the thin film on Si and SiO₂ is about 0.6 nm thinner than that on MgO and Al₂O₃. It is possible that this results from the interdiffusion of Si and Pt. We can not draw conclusions from the density of Pt in the thin films considering that the position of critical angle can not be fitted accurately in Fig.III.3 (c) and Fig.III.3 (d). The deviation at the critical angle means that the Parratt formalism can not be well applied and the density calculated in fitting is not credible.

Substrate	Si	SiO ₂	MgO	Al ₂ O ₃
Roughness of Pt (nm)	0.3	0.3	0.6	0.4
Roughness of interface (nm)	0.3	0.2	0.6	0.4
Density of Pt (g/cm ³)	21.4	21.0	20.5	21.4
Thickness of Pt (nm)	9.2	9.1	9.7	9.7

Table III.2: Structural parameters of as-deposited samples deduced from the simulation of the XRR data

After annealing of Pt/Si and Pt/Al₂O₃, the AFM measurement result is shown in Fig.III.4. The Pt/Si sample undergoes obvious dewetting (Fig.III.4 (a)). The roughness augments to $3.70 \pm 0.09 \text{ nm}$. Grains and holes with a diameter of about 10 nm are distributed on the surface. As is shown at larger scale (Fig.III.4 (b)), the distribution of the grains and holes is homogeneous and no other special structure is observed on the surface. Considering that the thickness of Pt thin film is 9.2 nm before annealing and the height difference on the AFM images is more than 16nm, we guess that there is no more thin film and the substrate is exposed in the holes. This guess shall be verified latter. In contrast, we do not observe

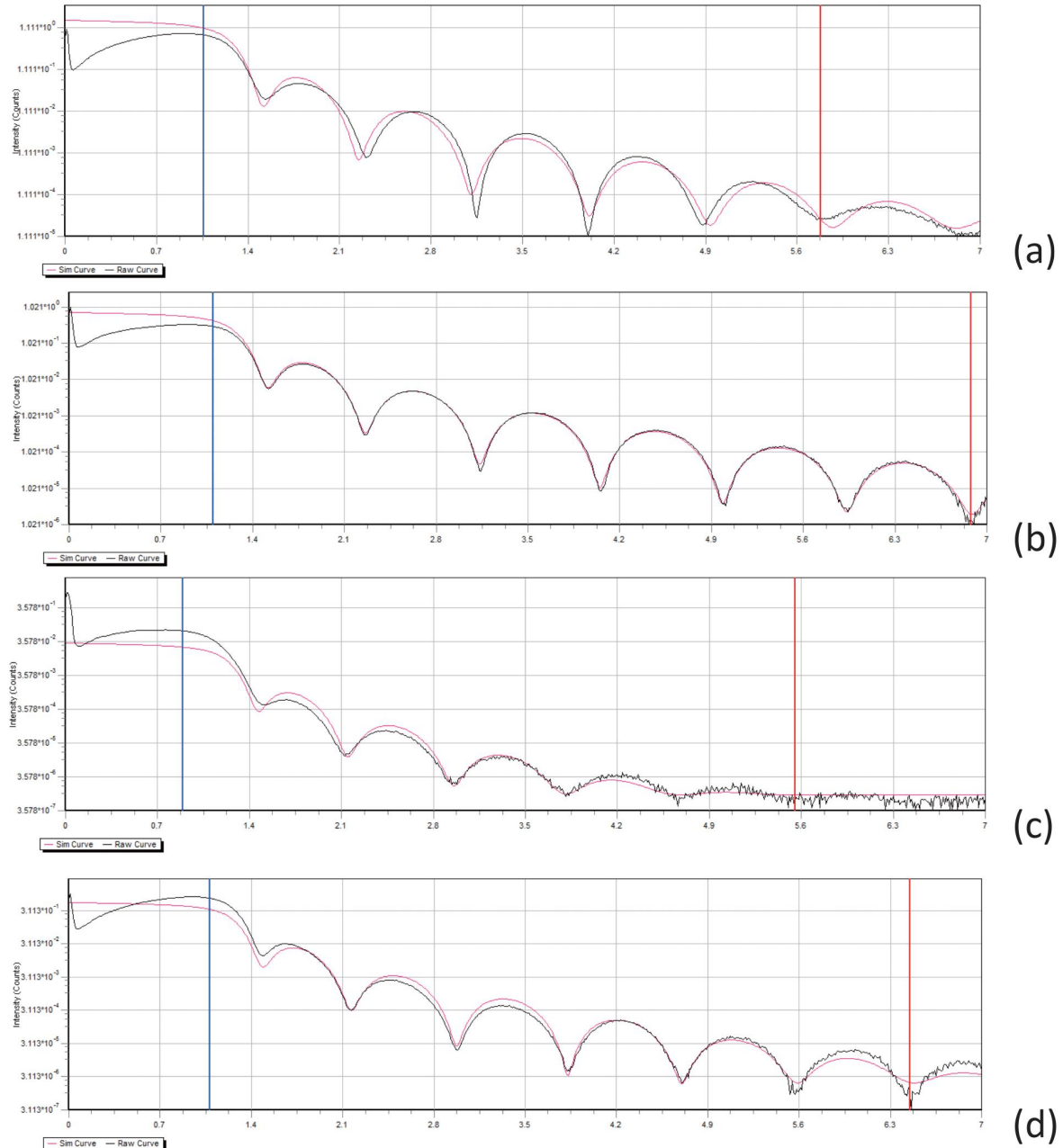


Figure III.3: Structural parameters of as-deposited samples deduced from the simulation of the XRR data : (a) Pt/Si (b) Pt/SiO₂ (c) Pt/MgO (d) Pt/Al₂O₃

dewetting on the Pt/Al₂O₃ sample (Fig.III.4 (c)). The roughness after annealing of Pt/Al₂O₃ is 0.40 ± 0.09 nm, which is very close to that before annealing. The annealing of Pt/SiO₂ and Pt/MgO could not be studied for lack of time, but earlier reports show that there is also dewetting for Pt/SiO₂ [36].

XRR measurement results after annealing are shown in Fig.III.5. There is no oscillation on XRR pattern of Pt/Si and we can not do the fitting of this curve (Fig.III.5 (a)). This means that there is no more thin film on the substrate. The curve vanishes at very small angle compared with other XRR patterns, which confirms that the surface is very rough. In contrast, the XRR pattern of annealed Pt/Al₂O₃ can be better fitted than before annealing (Fig.III.5

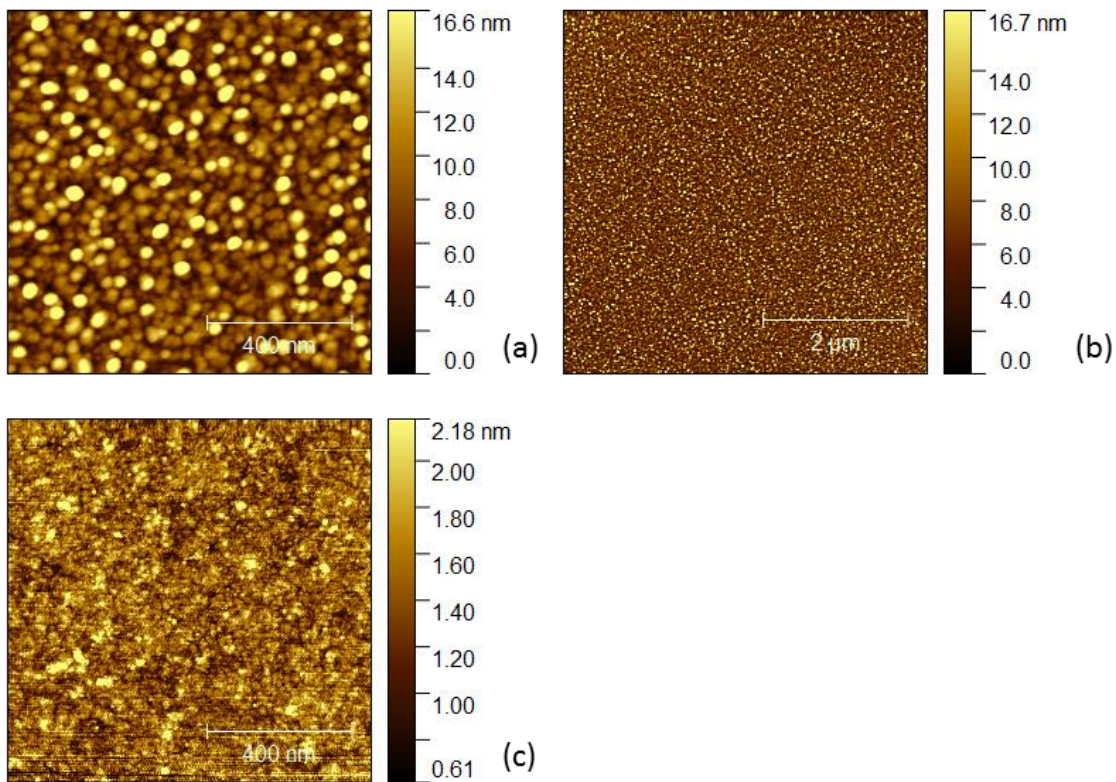


Figure III.4: AFM images of samples after annealing at 700 K for 30 min : (a) Pt/Si, 1 $\mu\text{m} \times 1 \mu\text{m}$ (b) Pt/Si, 5 $\mu\text{m} \times 5 \mu\text{m}$ (c) Pt/ Al_2O_3 , 1 $\mu\text{m} \times 1 \mu\text{m}$

(b)). This demonstrates that the structure of the thin film is more consistent with the model supposed in Parratt formalism. The parameters deduced from the simulation of XRR data are shown in Table.III.3. The uncertainty is the same as before, 0.1 nm for roughness and thickness and 0.1 g/cm³ for density. As we can see, the thickness does not change after annealing. The roughness of Pt thin film and the interface decreases a little.

Substrate	Roughness of Pt (nm)	Roughness of interface (nm)	Density of Pt (g/cm ³)	Thickness of Pt (nm)
Si	-	-	-	-
Al_2O_3	0.2	0.2	21.4	9.7

Table III.3: Structural parameters of annealed samples deduced from the simulation of the XRR data

Dewetting depends on the surface free energy per unit area. This energy is determined by the nature of the thin film, of the substrate as well as the energy of interaction between them. For films or islands (if there is dewetting) with isotropic surface energy per unit area γ_f , on a rigid substrate with surface energy per area γ_s and if the energy per area of the island-substrate interface is γ_i , energy minimization for a fixed volume gives the Young-Laplace equation :

$$\gamma_s = \gamma_i + \gamma_f \cos\theta$$

where θ is the equilibrium contact angle. If we have $\gamma_s > \gamma_i + \gamma_f$, the film is stable and there is no dewetting [37]. Documents show that the surface free energy of Si (0.9 J/m²) and SiO_2

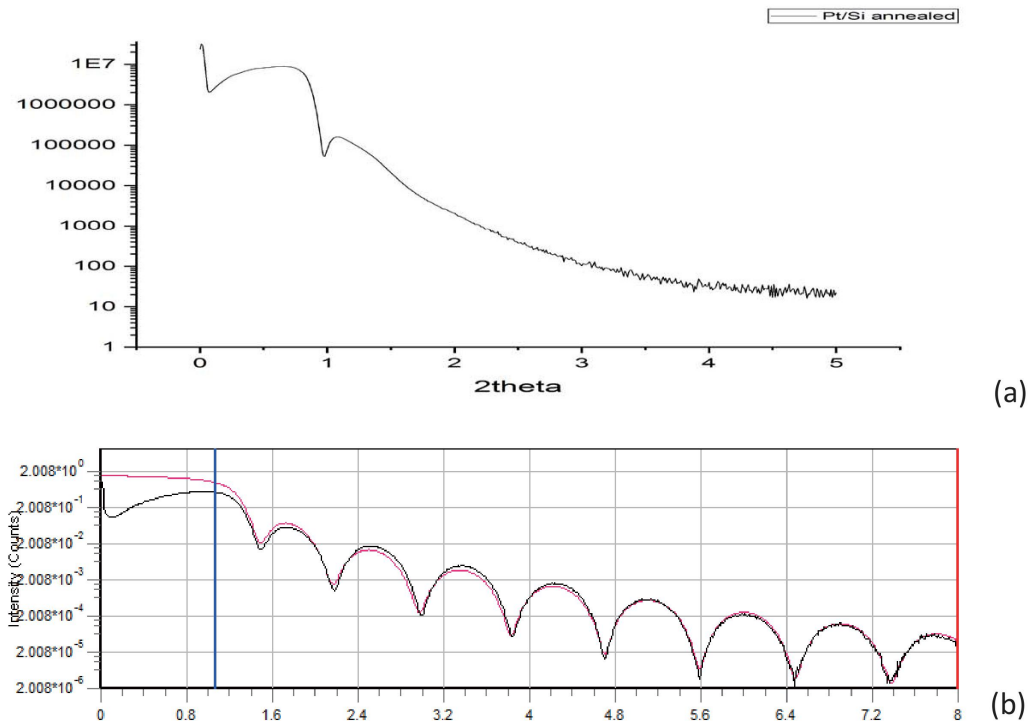


Figure III.5: Structural parameters of samples deduced from the simulation of the XRR data after annealing at 700 K for 30 min : (a) Pt/Si (b) Pt/Al₂O₃

is much smaller than Pt (2.2 J/m^2), while that of MgO (1.3 J/m^2) and Al₂O₃ is closer to Pt [38, 39]. The big difference of surface free energy between the thin film and the substrate leads to $\gamma_s < \gamma_f$. Therefore it is more likely to have dewetting on Si and SiO₂, although we do not know γ_i . Our experiments on Pt/Si and Pt/Al₂O₃ correspond to the theory, and it is highly possible that the dewetting of Pt is not important on MgO.

III.2 Crystal structure

Samples are characterized with symmetrical and grazing X-ray diffraction after the deposition. The symmetrical patterns are shown in Fig III.6. Substrate peaks are so high that we have to show the figure in logarithmic scale. Peaks of MgO(111), MgO(222), Al₂O₃(006), Al₂O₃(0 0 12), Si(400) and several lower-intensity peaks of these three substrates are found. No peak of SiO₂ is visible. According to our database, SiO₂ has many peaks and the intensity of these peaks is weak, so it is possible that the peaks of SiO₂ are hidden in background noise. The Cu X-ray source is kept in a W chamber and the chamber emits some X-rays, too. The supplementary X-rays result in some peaks that we do not want, for instance the peak of Si at 61.7° and probably the peaks of Al₂O₃ and MgO at 47.0° and at 55.9° . The substrate peaks are very sharp and the FWHM (full width at half maximum) is smaller than 0.05° . For Pt, we mainly see Pt(111) at 39.8° and Pt(222) at 85.7° . (222) is the second order of (111) plane. We conclude that textured Pt with the (111) plane parallel to the substrate surface is grown by sputtering deposition. The FWHM of Pt on four substrates is about 1° . The FWHM is sensitive to the variation in microstructure and strain accumulation in the material. We do not know which factor is more important in our sample, but it is clear that the Pt thin films

are not as high quality as the substrates since the FWHM is larger.

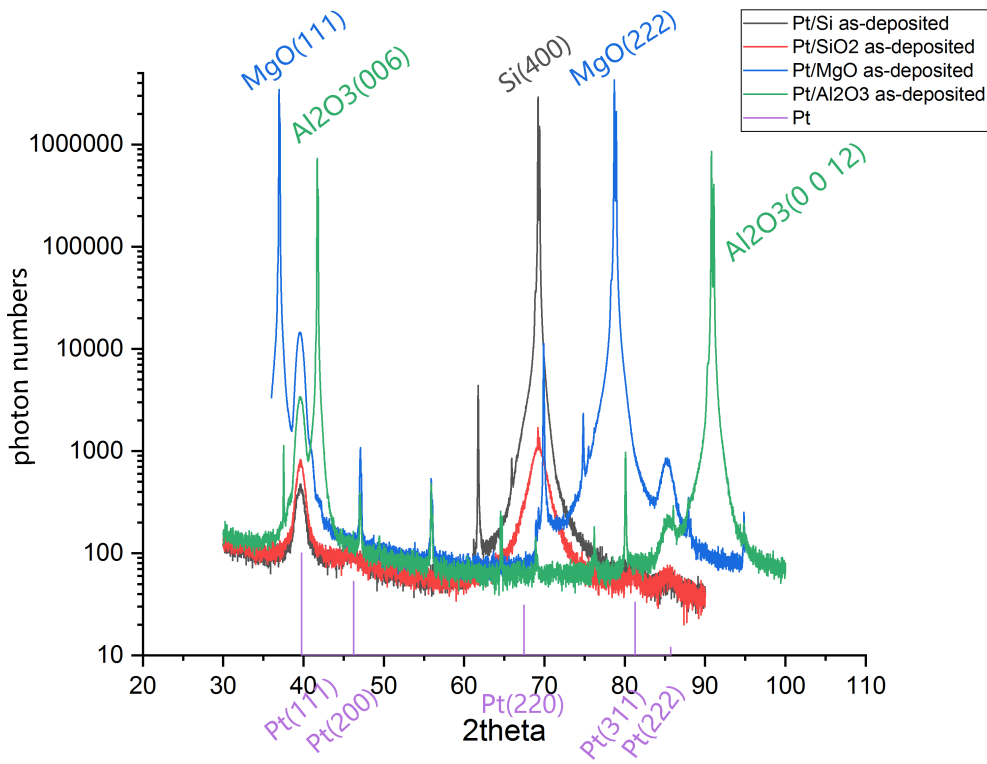


Figure III.6: Symmetrical diffraction patterns after the deposition in logarithmic scale

To perform the grazing diffraction experiment, we need to choose an incident angle which is a little larger than the critical angle of total reflection. The critical angle depends on the density of the surface. For Pt the critical angle is about 0.8° and we take 1.5° as the incident angle. It is possible to calculate the penetration depth of X-ray beam, τ . The penetration depth is defined as the depth at which the intensity of the radiation inside the material falls to $1/e$ of its original value at the surface. First we calculate the optical path length :

$$I = I_0 \exp\left(-\frac{\mu}{\rho} \rho L\right)$$

where L is the optical path length, μ/ρ is the mass attenuation coefficient, I is the intensity of X-ray beam and ρ is the density of the element, so density of Pt in our experiments. The mass attenuation coefficient varies according to the energy of photon. In our experiments, the wavelength is 0.15418 nm so the energy is 8.46 keV . The corresponding mass attenuation coefficient of Pt is $1.594 \times 10^2 \text{ cm}^2/\text{g}$ [40]. We should calculate L so that $I = I_0/e$. Therefore the optical path length is about $291 \pm 10 \text{ nm}$. Then we can calculate the penetration depth, τ :

$$\tau = 0.5L \sin\theta$$

where θ is the incident angle. The incident angle is 1.5° . Therefore the penetration depth is $3.8 \pm 0.1 \text{ nm}$. The X-ray beam does not reach the substrate as the thickness of the thin films is more than 9 nm .

The grazing diffraction pattern is shown in Fig.III.7. All the peaks of Pt in this range, including Pt(111) at 39.8° , Pt(200) at 46.2° , Pt(220) at 67.5° , Pt(311) at 81.3° and Pt(222)

at 85.7° are found in the patterns. In the patterns of Pt/Si and Pt/SiO₂ there are several peaks between 50° and 60°. This is because these two samples are too thin while the incident beam is relatively large. When the incident angle is small, the X-ray beam reaches the edges of Si and SiO₂ substrates. We can see Si(311) peak at 56.1°.

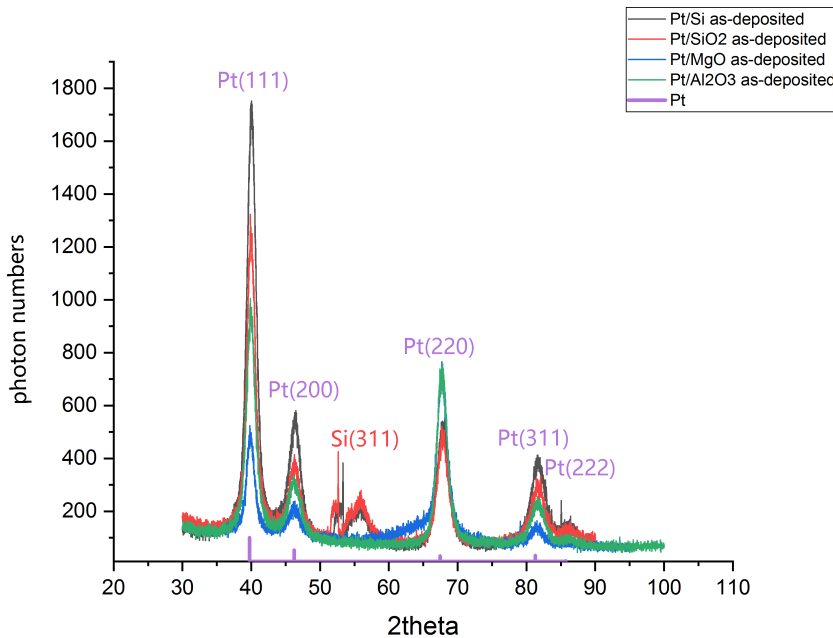


Figure III.7: Grazing diffraction patterns after the deposition

The Pt/Si sample changes a lot after annealing. The symmetrical diffraction patterns before and after annealing are shown in Fig.III.8. The figure is still in logarithmic scale as the peak of substrate is very high. There are two wide peaks between 43° and 46°. These peaks correspond to PtSi(211) at 43.9° and PtSi(202) at 44.6°. PtSi has more than twenty peaks in this range and the intensity of most peaks are weak, so it is possible that some peaks are hidden in background noise and we can not conclude about the orientation of PtSi. The peaks of Pt are no longer visible. The other peaks are from X-ray diffraction of Si, especially the peak of Si(400) which is the highest before and after the annealing. The existence of PtSi and the disappearance of Pt reveal that interdiffusion between Pt and Si happens during annealing.

The grazing diffraction patterns of Pt/Si before and after annealing are shown in Fig.III.9. As is mentioned before, PtSi has more than twenty peaks in this range and it is difficult to distinguish every peak when the peaks are wide. We can only distinguish several peaks of PtSi : PtSi(211) at 43.9°, PtSi(202) at 44.6°, PtSi(103) at 48.9°, PtSi(220) at 61.4°, PtSi(411) at 74.8° and PtSi(105) at 83.3°. Since we only see PtSi and do not see Pt in grazing diffraction pattern, we deduce that the interdiffusion is so severe that the whole thin film changes its composition. The peaks of Si substrate edge between 50° and 60° are still visible, but there is one intense peak of Si(311) at 56.1° in the pattern after annealing. This means that the X-ray beam reaches the Si substrate surface. We have observed holes in AFM images (Fig.III.4 (a) and (b)), so according to grazing diffraction patterns we confirm that the holes are deep enough to expose the substrate. The thin film is destroyed during annealing.

Symmetrical diffraction patterns of Pt/Al₂O₃ are shown in Fig.III.10. After annealing we still see the peaks of substrate, Al₂O₃(006) and Al₂O₃(0 0 12). For Pt, only Pt(111) and

PART III. RESULTS AND DISCUSSION

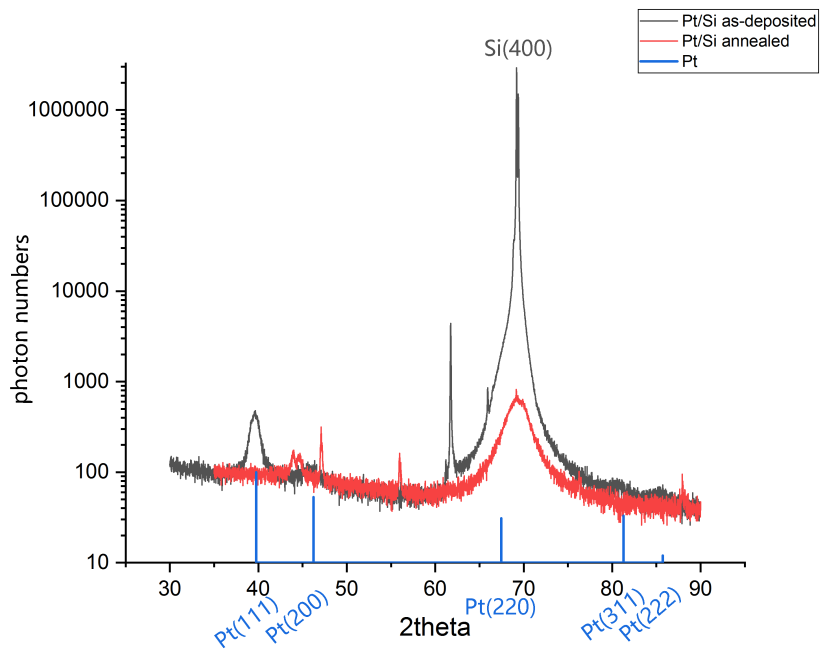


Figure III.8: Symmetrical diffraction patterns of Pt/Si in logarithmic scale

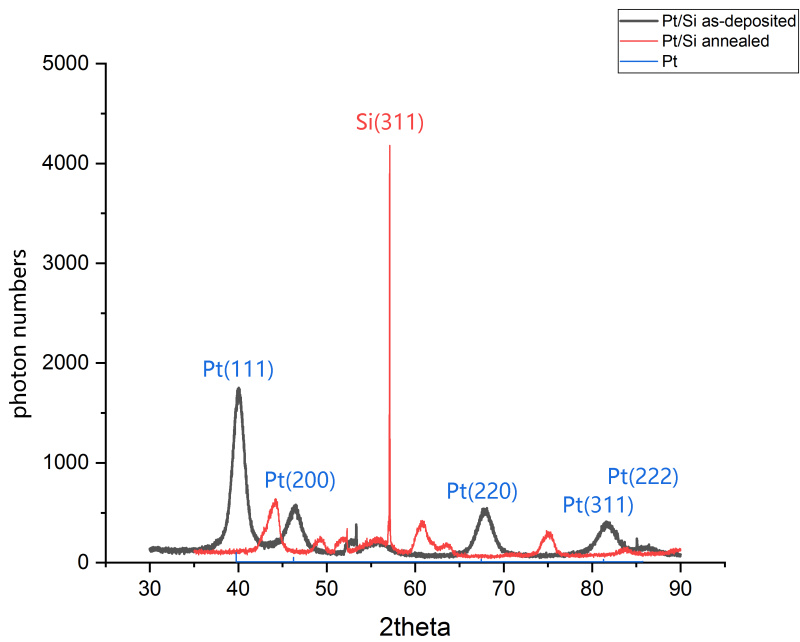


Figure III.9: Grazing diffraction patterns of Pt/Si

Pt(222) are observed. There are oscillations around these two peaks in the pattern after annealing. We count eight oscillations from $2\theta_0 = 32.2919^\circ$ to $2\theta_8 = 39.8581^\circ$. Then we calculate according to Bragg's law :

$$8\lambda = 2d(\sin\theta_8 - \sin\theta_0)$$

where λ is the wavelength of our diffractometer. It equals to 0.15418 nm. This calculation

leads to a distance, $d = 9.8 \pm 0.1$ nm. It is consistent with the thickness deduced from the simulation of the XRR data. This means that the thickness of the thin film is extremely well defined, and the lattice planes distribution as well, so that the interferences between X-rays scattered by Pt surface and Al₂O₃ substrate are observed. This is a striking effect of annealing. In the grazing diffraction patterns (Fig.III.11), we still observe Pt(111), Pt(200), Pt(220), Pt(311) and Pt(222) after annealing. No other peak is found. This means that no interdiffusion happens at the top of the thin film.

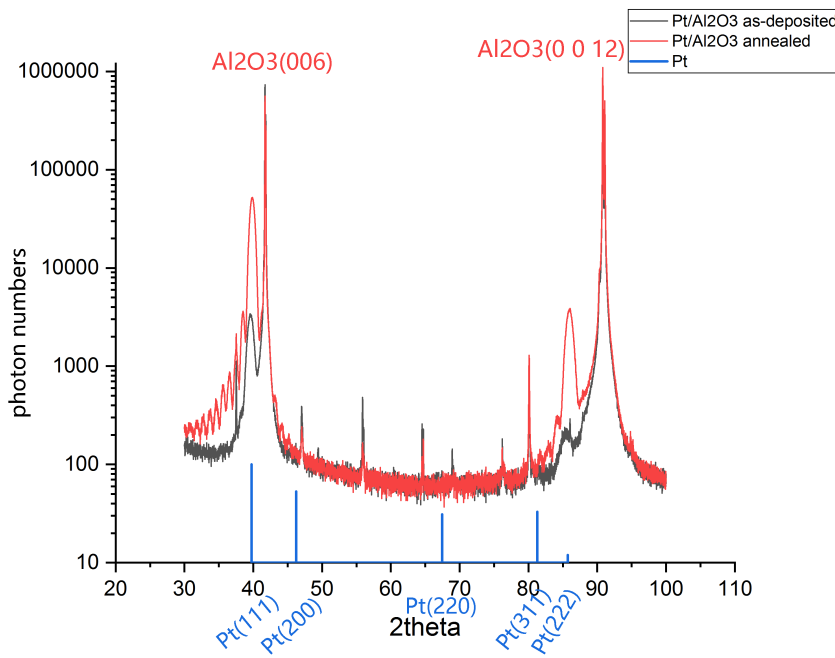


Figure III.10: Symmetrical diffraction patterns of Pt/Al₂O₃ in logarithmic scale

As the annealed Pt/Al₂O₃ seems to be highly crystallized according to symmetrical and grazing diffraction pattern, we want to know more about the relative orientation of the lattices within the surface plane by doing a phi scan. The phi scan should be done on a plane non-parallel to Pt(111) and Pt(222). The directions of (111), the other plane and the possible incident beam in reciprocal space are shown in Fig.III.12. θ is the angle of diffraction which is available in our database and α is the angle between (111) and the plane we choose. We need to make sure that $\theta > \alpha$, otherwise there can not be an incident beam. Besides, the intensity of all the peaks is known in the database and it is better to do the phi scan on a plane whose peak intensity is strong. If the peak intensity is weak, it will be difficult to distinguish the peak from background noise. According to our calculation, the angle α between Pt(311) and Pt(111) is 29.50° and in the database θ equals to 40.65°. The peak intensity of Pt(311) is relatively strong. Consequently we do the phi scan on Pt(311) and the incident angle is 11.15°, the result of $\theta - \alpha$.

The phi scan result is shown in Fig.III.13. According to the phi scan pattern, Pt(311) is periodically oriented and the period is 60°. This reflects the six-fold symmetry of the Pt(111) atomic planes. Therefore we conclude that the Pt thin film on Al₂O₃ substrate after annealing is highly epitaxial.

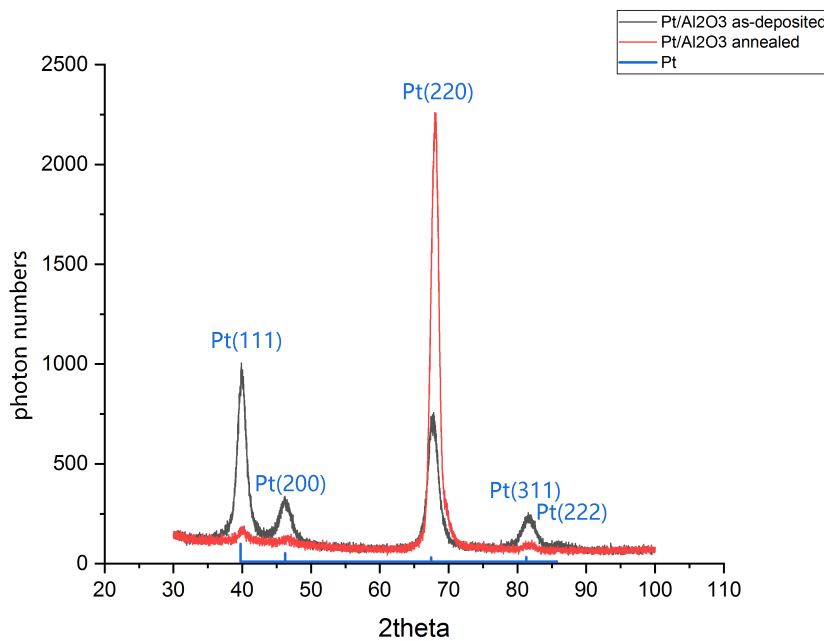


Figure III.11: Grazing diffraction patterns of Pt/Al₂O₃

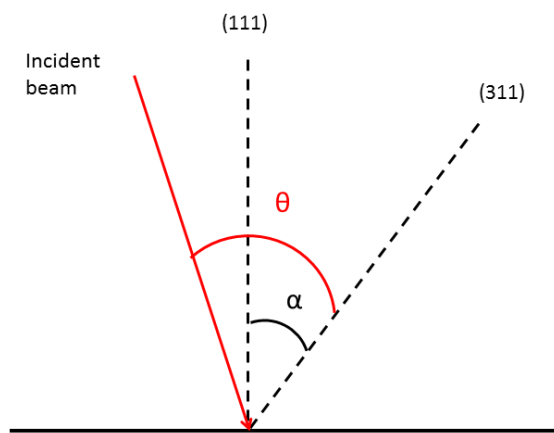


Figure III.12: How we decide the direction of phi scan

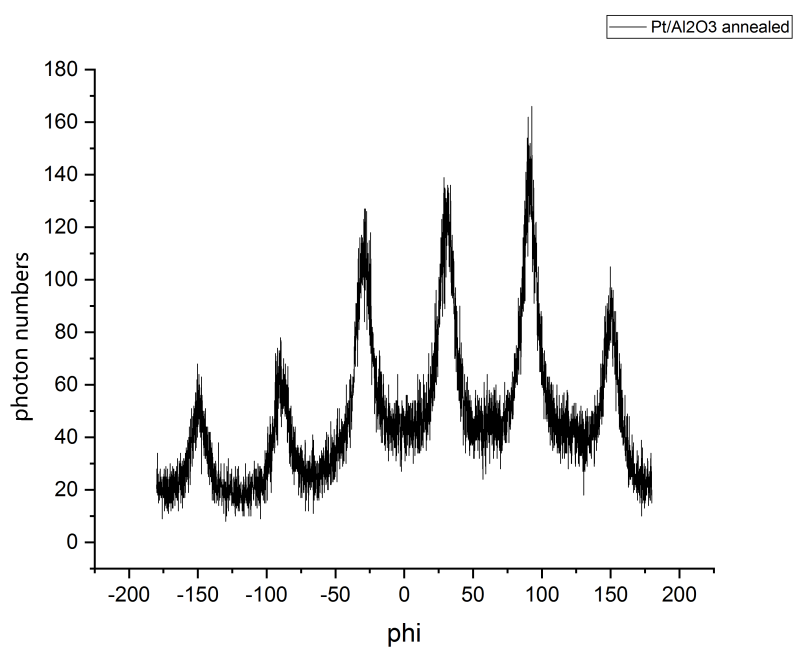


Figure III.13: Phi scan patterns of annealed Pt/Al₂O₃

Conclusion

The possibility to replace the bulk single-crystal Pt(111) with an epitaxial high quality Pt(111) thin film prepared on a commercial substrate for graphene CVD growth is studied. AFM measurements show that the substrates are flat before any treatment. Linear traces are observed on the surface of MgO. Then Pt thin films with the thickness of 10 nm are grown on MgO(111), Al₂O₃(0001), SiO₂(2 nm)(001)/Si and SiO₂(300 nm)(001)/Si substrates by sputtering deposition. AFM and XRR characterization show that the thin films are very homogeneous and the roughness of the surface is low. The linear traces on Pt/MgO are still observed. XRR measurements and simulations demonstrate that the Pt thin film on SiO₂(2 nm)(001)/Si and SiO₂(300 nm)(001)/Si is 0.6 nm thinner than the other two samples, which may be due to interdiffusion between Pt and Si. The Pt/SiO₂(2 nm)(001)/Si and Pt/Al₂O₃(0001) samples are annealed in ultrahigh vacuum at 700K for 30 min. Severe dewetting is observed on Pt/SiO₂(2 nm)(001)/Si sample. Grazing XRD measurement shows that there is only PtSi on the surface and the Si substrate is exposed. Therefore because of dewetting and interdiffusion the Pt thin film evolves into PtSi islands. In contrast, the annealed Pt/Al₂O₃(0001) is still flat. Symmetrical diffraction reveals that the thin film is well defined with the (111) plane parallel to the substrate. No interdiffusion is observed on the surface of this sample. Finally, phi scan XRD shows that high quality epitaxial Pt(111) thin film is obtained by annealing.

For further studies, on the one hand, graphene CVD growth should be done on Pt//Al₂O₃(0001) to verify if the graphene grown is of high quality, which is important for graphene/Co/Pt(111) preparation. On the other hand, it is known that SiO₂(300 nm)(001)/Si is not a good substrate according to previous studies but the MgO(111) substrate is not studied. Annealing and characterization of Pt/MgO(111) should be done.

Bibliography

- [1] Andre K Geim and Konstantin S Novoselov. The rise of graphene. In *Nanoscience and Technology: A Collection of Reviews from Nature Journals*, pages 11–19. World Scientific, 2010.
- [2] Daniel Huertas-Hernando, F Guinea, and Arne Brataas. Spin-orbit coupling in curved graphene, fullerenes, nanotubes, and nanotube caps. *Physical Review B*, 74(15):155426, 2006.
- [3] Nikolaos Tombros, Csaba Jozsa, Mihaita Popinciuc, Harry T Jonkman, and Bart J Van Wees. Electronic spin transport and spin precession in single graphene layers at room temperature. *Nature*, 448(7153):571, 2007.
- [4] Wei Han, Roland K Kawakami, Martin Gmitra, and Jaroslav Fabian. Graphene spintronics. *Nature nanotechnology*, 9(10):794, 2014.
- [5] Wei Han, K Pi, Kathleen M McCreary, Yan Li, Jared JI Wong, AG Swartz, and RK Kawakami. Tunneling spin injection into single layer graphene. *Physical review letters*, 105(16):167202, 2010.
- [6] David Soriano, Nicolas Leconte, Pablo Ordejón, Jean-Christophe Charlier, Juan-Jose Palacios, and Stephan Roche. Magnetoresistance and magnetic ordering fingerprints in hydrogenated graphene. *Physical review letters*, 107(1):016602, 2011.
- [7] Igor Žutić, Jaroslav Fabian, and S Das Sarma. Spintronics: Fundamentals and applications. *Reviews of modern physics*, 76(2):323, 2004.
- [8] Martin Weser, EN Voloshina, Karsten Horn, and Yu S Dedkov. Electronic structure and magnetic properties of the graphene/fe/ni (111) intercalation-like system. *Physical Chemistry Chemical Physics*, 13(16):7534–7539, 2011.
- [9] Nicolas Rougemaille, AT N'Diaye, Johann Coraux, Chi Vo-Van, Olivier Fruchart, and AK Schmid. Perpendicular magnetic anisotropy of cobalt films intercalated under graphene. *Applied Physics Letters*, 101(14):142403, 2012.
- [10] Fernando Ajejas, Adrian Gudín, Ruben Guerrero, Miguel Angel Niño, Stefania Pizzini, Jan Vogel, Manuel Valvidares, Pierluigi Gargiani, Mariona Cabero, Maria Varela, et al. Unravelling dzyaloshinskii-moriya interaction and chiral nature of graphene/cobalt interface. *arXiv preprint arXiv:1803.07443*, 2018.
- [11] Johann Coraux, Alpha T N'Diaye, Nicolas Rougemaille, Chi Vo-Van, Amina Kimouche, Hong-Xin Yang, Mairbek Chshiev, Nedjma Bendiab, Olivier Fruchart, and Andreas K Schmid. Air-protected epitaxial graphene/ferromagnet hybrids prepared by chemical vapor deposition and intercalation. *The Journal of Physical Chemistry Letters*, 3(15):2059–2063, 2012.
- [12] RS Mane and CD Lokhande. Chemical deposition method for metal chalcogenide thin films. *Materials Chemistry and Physics*, 65(1):1–31, 2000.
- [13] GA Prinz and JJ Krebs. Molecular beam epitaxial growth of single-crystal fe films on gaas. *Applied Physics Letters*, 39(5):397–399, 1981.
- [14] Chang-Wook Jeong, Jang-Sik Lee, and Seung-Ki Joo. Plasma-assisted atomic layer growth of high-quality aluminum oxide thin films. *Japanese Journal of Applied Physics*, 40(1R):285, 2001.
- [15] Masahiro Akiyama, Yoshihiro Kawarada, Takashi Ueda, Seiji Nishi, and Katsuzo Kamimishi. Growth of high quality gaas layers on si substrates by mocvd. *Journal of Crystal Growth*, 77(1-3):490–497, 1986.
- [16] Yoshiaki Suda, Hiroharu Kawasaki, Tsuyoshi Ueda, and Tamiko Ohshima. Preparation of high quality nitrogen doped tio₂ thin film as a photocatalyst using a pulsed laser deposition method. *Thin solid films*, 453:162–166, 2004.
- [17] Yalan Hu, Xungang Diao, Cong Wang, Weichang Hao, and Tianmin Wang. Effects of heat treatment on properties of ito films prepared by rf magnetron sputtering. *Vacuum*, 75(2):183–188, 2004.
- [18] Walter Water and Sheng-Yuan Chu. Physical and structural properties of zno sputtered films. *Materials Letters*, 55(1-2):67–72, 2002.
- [19] Vinay Gupta and Abhai Mansingh. Influence of postdeposition annealing on the structural and optical properties of sputtered zinc oxide film. *Journal of Applied Physics*, 80(2):1063–1073, 1996.

BIBLIOGRAPHY

- [20] Lin Cui, Hua-Yu Zhang, Gui-Gen Wang, Fang-Xu Yang, Xu-Ping Kuang, Rui Sun, and Jie-Cai Han. Effect of annealing temperature and annealing atmosphere on the structure and optical properties of zno thin films on sapphire (0 0 1) substrates by magnetron sputtering. *Applied Surface Science*, 258(7):2479–2485, 2012.
- [21] JW Lee, H Shichijo, HL Tsai, and RJ Matyi. Defect reduction by thermal annealing of gaas layers grown by molecular beam epitaxy on si substrates. *Applied Physics Letters*, 50(1):31–33, 1987.
- [22] BM Lairson, MR Visokay, R Sinclair, S Hagstrom, and BM Clemens. Epitaxial pt (001), pt (110), and pt (111) films on mgo (001), mgo (110), mgo (111), and al₂o₃ (0001). *Applied physics letters*, 61(12):1390–1392, 1992.
- [23] Xuesong Li, Weiwei Cai, Jinho An, Seyoung Kim, Junghyo Nah, Dongxing Yang, Richard Piner, Aruna Velamakanni, Inhwa Jung, Emanuel Tutuc, et al. Large-area synthesis of high-quality and uniform graphene films on copper foils. *science*, 324(5932):1312–1314, 2009.
- [24] Hiroki Ago, Yoshito Ito, Noriaki Mizuta, Kazuma Yoshida, Baoshan Hu, Carlo M Orofeo, Masaharu Tsuji, Ken-ichi Ikeda, and Seigi Mizuno. Epitaxial chemical vapor deposition growth of single-layer graphene over cobalt film crystallized on sapphire. *Acs Nano*, 4(12):7407–7414, 2010.
- [25] PW Sutter, PM Albrecht, and Eli A Sutter. Graphene growth on epitaxial ru thin films on sapphire. *Applied Physics Letters*, 97(21):213101, 2010.
- [26] Takayuki Iwasaki, Hye Jin Park, Mitsuharu Konuma, Dong Su Lee, Jurgen H Smet, and Ulrich Starke. Long-range ordered single-crystal graphene on high-quality heteroepitaxial ni thin films grown on mgo (111). *Nano letters*, 11(1):79–84, 2010.
- [27] Kongara M Reddy, Andrew D Gledhill, Chun-Hu Chen, Julie M Drexler, and Nitin P Padture. High quality, transferrable graphene grown on single crystal cu (111) thin films on basal-plane sapphire. *Applied Physics Letters*, 98(11):113117, 2011.
- [28] Keun Soo Kim, Yue Zhao, Houk Jang, Sang Yoon Lee, Jong Min Kim, Kwang S Kim, Jong-Hyun Ahn, Philip Kim, Jae-Young Choi, and Byung Hee Hong. Large-scale pattern growth of graphene films for stretchable transparent electrodes. *nature*, 457(7230):706, 2009.
- [29] Peter Sutter, Jerzy T Sadowski, and Eli Sutter. Graphene on pt (111): Growth and substrate interaction. *Physical Review B*, 80(24):245411, 2009.
- [30] M Enachescu, D Schleef, DF Ogletree, and M Salmeron. Integration of point-contact microscopy and atomic-force microscopy: Application to characterization of graphite/pt (111). *Physical Review B*, 60(24):16913, 1999.
- [31] Elena Loginova, Shu Nie, Konrad Thürmer, Norman C Bartelt, and Kevin F McCarty. Defects of graphene on ir (111): Rotational domains and ridges. *Physical Review B*, 80(8):085430, 2009.
- [32] PA Khomyakov, G Giovannetti, PC Rusu, G vd Brocks, J Van den Brink, and Paul J Kelly. First-principles study of the interaction and charge transfer between graphene and metals. *Physical Review B*, 79(19):195425, 2009.
- [33] M Gao, Y Pan, L Huang, H Hu, LZ Zhang, HM Guo, SX Du, and H-J Gao. Epitaxial growth and structural property of graphene on pt (111). *Applied Physics Letters*, 98(3):033101, 2011.
- [34] Hirokazu Ueta, Morihiko Saida, Chikara Nakai, Yoichi Yamada, Masahiro Sasaki, and Shigehiko Yamamoto. Highly oriented monolayer graphite formation on pt (1 1 1) by a supersonic methane beam. *Surface science*, 560(1-3):183–190, 2004.
- [35] VL Mironov, OG Udalov, BA Gribkov, and AA Fraerman. Comparative x-ray reflectometry and atomic force microscopy of surfaces with non-gaussian roughness. *Journal of Applied Physics*, 104(6):064301, 2008.
- [36] Ji-Myon Lee and Byung-II Kim. Thermal dewetting of pt thin film: Etch-masks for the fabrication of semiconductor nanostructures. *Materials Science and Engineering: A*, 449:769–773, 2007.
- [37] Carl V Thompson. Solid-state dewetting of thin films. *Annual Review of Materials Research*, 42:399–434, 2012.
- [38] WR Tyson and WA Miller. Surface free energies of solid metals: Estimation from liquid surface tension measurements. *Surface Science*, 62(1):267–276, 1977.
- [39] Masashi Nakamoto, Akihito Kiyose, Toshihiro Tanaka, Lauri Holappa, and Marko Hämäläinen. Evaluation of the surface tension of ternary silicate melts containing al₂o₃, cao, feo, mgo or mno. *ISIJ international*, 47(1):38–43, 2007.
- [40] John H Hubbell and Stephen M Seltzer. Tables of x-ray mass attenuation coefficients and mass energy-absorption coefficients 1 kev to 20 mev for elements z= 1 to 92 and 48 additional substances of dosimetric interest. Technical report, National Inst. of Standards and Technology-PL, Gaithersburg, MD (United States). Ionizing Radiation Div., 1995.

Glossary

AFM Atomic force microscopy

ALD Atomic layer deposition

ARPES Angle resolved photoemission spectroscopy

CBD Chemical bath deposition

CVD Chemical vapour deposition

DMI Dzyaloshinskii-Moriya interaction

FM Frank-van der Merwe mode

FM Ferromagnetic

LEED Low-energy electron diffraction

LEEM Low-energy electron microscopy

MBE Molecular beam epitaxy

MOCVD Metalorganic chemical vapour deposition

RHEED Reflection high-energy electron diffraction

SK Stranski-Krastanov mode

STM Scanning tunneling microscope

VW Volmer-Weber mode

XRD X-ray diffraction

XRR X-ray reflectivity

List of Tables

III.1	Roughness (rms) of the samples in different status (nm)	21
III.2	Structural parameters of as-deposited samples deduced from the simulation of the XRR data	23
III.3	Structural parameters of annealed samples deduced from the simulation of the XRR data	25

List of Figures

I.1	Roughness after annealed at different temperatures	11
I.2	Mono-layer graphene growth on Pt(111)	13
I.3	Single-domain micro-LEED patterns of mono-layer graphene on Pt(111)	14
I.4	STM images of graphene grown on Pt(111)	15
II.1	Sputtering deposition	16
II.2	Atomic force microscope	17
II.3	X-ray diffraction	19
II.4	X-ray reflectivity	19
II.5	Experiment process	20
III.1	AFM images before deposition	22
III.2	AFM images after deposition	22
III.3	Structural parameters of as-deposited samples deduced from the simulation of the XRR data	24
III.4	AFM images after annealing	25
III.5	Structural parameters of annealed samples deduced from the simulation of the XRR data	26
III.6	Symmetrical diffraction patterns after the deposition	27
III.7	Grazing diffraction patterns after the deposition	28
III.8	Symmetrical diffraction patterns of Pt/Si	29
III.9	Grazing diffraction patterns of Pt/Si	29
III.10	Symmetrical diffraction patterns of Pt/Al ₂ O ₃	30
III.11	Grazing diffraction patterns of Pt/Al ₂ O ₃	31
III.12	The choice of phi scan direction	31
III.13	Phi scan patterns of annealed Pt/Al ₂ O ₃	32